BRNO UNIVERSITY OF TECHNOLOGY
VYSOKÉ UČENÍ TECHNICKÉ V BRNĚ

FACULTY OF MECHANICAL ENGINEERING
FAKULTA STROJNÍHO INŽENÝRSTVÍ

INSTITUTE OF PHYSICAL ENGINEERING
ÚSTAV FYZIKÁLNÍHO INŽENÝRSTVÍ

SPATIO-TEMPORAL DYNAMICS AND COHERENT CONTROL OF QUANTUM CASCADE LASER FREQUENCY COMBS

ČASOPROSTOROVÁ DYNAMIKA A KOHERENTNÍ ŘÍZENÍ FREKVENČNÍCH HŘEBENŮ KVANTOVÝCH KASKÁDOVÝCH LASERŮ

MASTER'S THESIS
DIPLOMOVÁ PRÁCE

AUTHOR — **Bc. Aleš Konečný**
AUTOR PRÁCE

SUPERVISOR — **Dr.techn. Ing. Hermann Detz**
VEDOUCÍ PRÁCE

BRNO 2021

BRNO UNIVERSITY OF TECHNOLOGY
FACULTY OF MECHANICAL ENGINEERING

Assignment Master's Thesis

Institut:	Institute of Physical Engineering
Student:	**Bc. Aleš Konečný**
Degree programm:	Physical Engineering and Nanotechnology
Branch:	no specialisation
Supervisor:	**Dr.techn. Ing. Hermann Detz**
Academic year:	2020/21

As provided for by the Act No. 111/98 Coll. on higher education institutions and the BUT Study and Examination Regulations, the director of the Institute hereby assigns the following topic of Master's Thesis:

Spatio–temporal dynamics and coherent control of quantum cascade laser frequency combs

Brief Description:

Frequency combs can be used to build spectrometers without any moving parts and thus are important building blocks for future monolithically integrated chemical sensors. The stability of the combs thereby plays a crucial role. Here, different concepts should be studied in order to mutually stabilize two combs. The spatio–temporal dynamics of quantum cascade laser frequency combs can be described by a travelling wave model.
The main challenge in simulating these lasers is the high computational demand. The available highly optimized simulation tool should be extended to account for coherent control techniques, such as electrical and optical injection locking.

Master's Thesis goals:

The available highly optimized simulation tool should be extended to account for coherent control techniques, such as electrical and optical injection locking.

Recommended bibliography:

HILLBRAND, Johannes, Aaron Maxwell ANDREWS, Hermann DETZ, Gottfried STRASSER, Benedikt SCHWARZ a Lukas NOVOTNY. Coherent injection locking of quantum cascade laser frequency combs. Nature Photonics. 2019, 13(2), 101-104. ISSN 1749-4885. Dostupné z: doi:10.1038/s41566-018-0320-3

OPAČAK, Nikola, Benedikt SCHWARZ, Hermann DETZ, Gottfried STRASSER, Benedikt SCHWARZ a Lukas NOVOTNY. Theory of Frequency-Modulated Combs in Lasers with Spatial Hole Burning, Dispersion, and Kerr Nonlinearity. Physical Review Letters. 2019, 123(24), 101-104. ISSN 0031-9007. Dostupné z: doi:10.1103/PhysRevLett.123.243902

Deadline for submission Master's Thesis is given by the Schedule of the Academic year 2020/21

In Brno,

L. S.

prof. RNDr. Tomáš Šikola, CSc.
Director of the Institute

doc. Ing. Jaroslav Katolický, Ph.D.
FME dean

Abstrakt

Kvantové kaskádové laserové frekvenční hřebeny jsou slibnými kandidáty pro nové miniaturizované spektrometry bez pohyblivých částí. Mohou být generovány v samočinném režimu pomocí různých nelinearit vyvolaných asymetrickým ziskem a vlnovodovou disperzí. K simulaci samočinných hřebenů byl použit dostupný vysoce optimalizovaný nástroj založený na modelu postupné vlny. Dále byl rozšířen o funkci zamykání optickým vstřikováním, koherentní techniky ovládání frekvenčních hřebenů. Následné simulace potvrdily uzamčení pomocí vstřikovaného signálu. Bylo zjištěno, že disperze grupové rychlosti (GVD) má významný dopad na rozsah zamykání. GVD byla vypočtena pro typické zařízení a frekvenční hřeben byl uzamčen pomocí optického vstřikování v rozsahu ladění od -2 do 47 MHz.

Summary

Quantum cascade laser frequency combs are promising candidates for novel miniaturized spectrometers without any moving parts. They can be generated in the self-starting regime by an interplay of different nonlinearities induced by asymmetrical gain and waveguide dispersion. The available highly optimized tool based on the traveling wave model was used to simulate the self-starting combs. It was further extended by the optical injection locking functionality, the coherent technique of control of frequency combs. Subsequent simulations confirmed locking to the injected signal. Group velocity dispersion (GVD) has been found to have a significant impact on the range of locking. GVD was calculated for the typical device and the frequency comb was optically injection-locked in a detuning range from -2 to 47 MHz.

Klíčová slova

kvantový kaskádový laser, frekvenční hřeben, disperze grupové rychlosti, zamykání optickým vstřikováním

Keywords

quantum cascade laser, frequency comb, group velocity dispersion, optical injection locking

KONEČNÝ, A. *Časoprostorová dynamika a koherentní řízení frekvenčních hřebenů kvantových kaskádových laserů.* Brno: Vysoké učení technické v Brně, Fakulta strojního inženýrství, 2021. 56 s. Supervisor Dr.techn. Ing. Hermann Detz.

I declare that I have elaborated my master's thesis on the theme "'Spatio-temporal dynamics and coherent control of quantum cascade laser frequency combs"' independently, under the supervision of master's thesis supervisor and with the use of technical literature and other sources of information which are all quoted in the thesis and detailed in the list of literature at the end of the thesis.

Bc. Aleš Konečný

I am very grateful to my supervisor Dipl-Ing. Dr.techn. Hermann Detz, for his time, effort, kindness, help and all valuable advices he has given to me. My thanks belong to MSc. Nikola Opacak, who guided me through the simulations, significantly helped with data evaluation and gave me valuable feedback to the thesis. I would also like to thank Dipl-Ing. Dr.techn. Benedikt Schwarz for devising entertaining theme of master's thesis and his technical support. Last but not least, I thank to my family and my girlfriend Kateřina Šuterová for their support and understanding during the difficult time of writing. I would also like to acknowledge, that this work was carried out with the support of the Institute of Solid-State Electronics at Technical University of Vienna.

Bc. Aleš Konečný

Contents

Introduction **3**

1 QCL frequency combs **5**
1.1 Mid-infrared region . . . 5
1.1.1 Spectroscopic methods . . . 5
1.2 Quantum cascade laser . . . 8
1.2.1 Laser fundamentals . . . 9
1.2.2 Laser cavity . . . 12
1.2.3 Active region . . . 16
1.2.4 Overall design . . . 17
1.3 Frequency combs . . . 18
1.3.1 Self-starting comb . . . 19
1.3.2 Injection locking . . . 20
1.3.3 Dual comb spectroscopy . . . 22

2 Instruments **25**
2.1 Travelling wave model . . . 25
2.1.1 Motivation . . . 25
2.1.2 Theory . . . 26
2.1.3 Numerical implementation . . . 28
2.2 Wave guiding model . . . 30

3 Simulations **33**
3.1 Self-starting frequency combs . . . 33
3.2 Wave guiding simulations . . . 37
3.3 Optical injection locking . . . 39

Summary **47**

Bibliography **49**

List of Abbreviations **56**

Introduction

Under the term laser, people usually see devices producing intense, spatially localized beam of electromagnetic (EM) field at a single frequency [1]. Although such a description is not wrong, it is more accurate to refer to them as to the devices with coherent optical output. This means, individual photons are tightly related to each other in terms of phase and amplitude in both space and time [2]. This criterion is fulfilled not only by single frequency devices, but also by frequency combs [3]. Optical frequency combs are lasers, whose spectrum consists of a set of modes, which act like a ruler in a frequency domain. They are evenly spaced and certainly phase related to each other [4], where a strictly defined phase relationship makes the difference between incoherent multi-mode laser and coherent frequency comb [3].

In literature, the generation of frequency combs is depicted as an instrument to obtain ultrashort pulses [1]. This has been demonstrated in the femtosecond regime by many groups [5] [6]. On the other hand, a comb spectrum is according to Fourier theorem generated by any periodic signal, regardless of its shape [4]. Hence, periodic continuous-wave (CW) frequency-modulated (FM) signal also generates frequency combs. Although, the first FM lasers date back to 1960s [7], the quantum cascade laser (QCL) community has not been extensively studying this field until 2012 [4], when it was first shown that QCL devices could be used to generate self-starting combs with approximately constant intensity output[8].

It is very important to mention, that QCLs emit in the mid-infrared (MIR) and terahertz (THz) portion of the spectrum, where many molecules can be identified through their unique pattern of absorption lines, resulted from the occurrence of rotational and vibrational states [9]. This can be used for applications in the field of chemical physics [10], chemistry [11], biology [12] and medicine [13]. Consequently, QCLs have been previously studied due to their potential for on-chip integration [14], high tunability [15] and relatively high output powers [16].

In 2014, QCL frequency combs were suggested for dual comb spectroscopy application [17]. Those spectrometers are very promising for on-chip integration, as they do not need any moving parts [17]. With the introduction of an attractive application, the demand for the comb engineering increased. Even though it is particularly beneficial to employ a reliable simulation tool, available methods could not faithfully display the physics behind FM combs [18].

In 2019 at Technical University of Vienna, a model based on the spatio-temporally resolved Maxwell-Bloch equations in the slowly varying envelope approximation has been developed [4, 19]. The response of the variables has not been assumed instantaneous, but expanded in a Taylor series and group velocity dispersion (GVD) with linewidth enhancement factor (LEF) effects have been implemented. This method

leading to the single master equation covers both the underlying physics behind FM generation and their most significant contributions [4]. The master equation was further numerically developed to create a highly optimized simulation tool, which is used in this thesis.

The main goal of this thesis is to get the big picture overview of the coherent FM techniques by studying both passive and active mode-locking techniques. The self starting conditions for comb generation will be simulated and use of coherent techniques for comb FM will be further developed and simulated, with the emphasis on the optical injection locking.

The first chapter gives an introduction to the QCL frequency combs, explaining the important principles behind this technology branch and pointing to similar approaches in MIR region. The second chapter deals with the simulation tools, from their theoretical background to the numerical application. In the third chapter, the results of self-starting combs and active modulation techniques are presented. Ultimately, a discussion is provided, putting the work behind the thesis into scientific context.

1. QCL frequency combs

The main goal of this chapter is to provide an overview about QCL frequency combs and to shed light on the underlying mechanisms behind their formation. It starts with the short presentation of the mid-infrared region, pointing out why are we so interested in this spectral region and explaining the demands for the laser and spectroscopic technology in this field. Next, QCLs are introduced and compared to other technological solutions, followed by a section about frequency combs. The last section is devoted to the comb spectroscopy studies with the emphasis on the dual comb spectroscopy, emerging competition for the conventionally used Fourier-transform infrared (FTIR) spectrometers and the most promising application of the MIR CW frequency combs.

1.1 Mid-infrared region

The infrared spectrum has only 3 three regions of atmosphere transparency. The first comes from the visible light to about 2.5 μm, the second covers the range from 3 to 5 μm and the last from 8 to 14 μm [9]. To be able to build high signal-to-noise ratio detectors outside vacuum, the measurement should take place in one of these transparency windows. Luckily, the MIR region includes the second and the third window as it covers the spectral range from 2.5 to 20 μm [20]. Furthermore, the whole region contains many vibrational and rotational molecular states (mostly fundamental) [9], represented by narrow optical absorption lines, as we see in figure 1.1.

Existence of these states is crucial for chemical sensing. A sample can be illuminated by a light source and from the absorption signal on a detector we can precisely determine the molecular content of the sample [9]. Moreover, we can estimate the concentration c from the Beer-Lambert law in eq. 1.1

$$A = \epsilon l c, \tag{1.1}$$

where A is the measured absorbance, l is the optical length and ϵ is the absorptivity, which is obtained from the material calibration measurement. Many commercial devices use this approach to determine the concentration of some specific gas, for example non-dispersive infrared CO_2 sensors [23]. Some researchers are also trying to use integrated laser sources and corresponding narrow-band detectors to reach small dimensions and high wall-plug efficiency [24].

1.1.1 Spectroscopic methods

In order to build a spectrometer, that is able to record broad spectra instead of single frequency information, some kind of frequency scanning is usually introduced. The most common approach is the FTIR spectroscopy. An FTIR spectroscopy uses incoherent

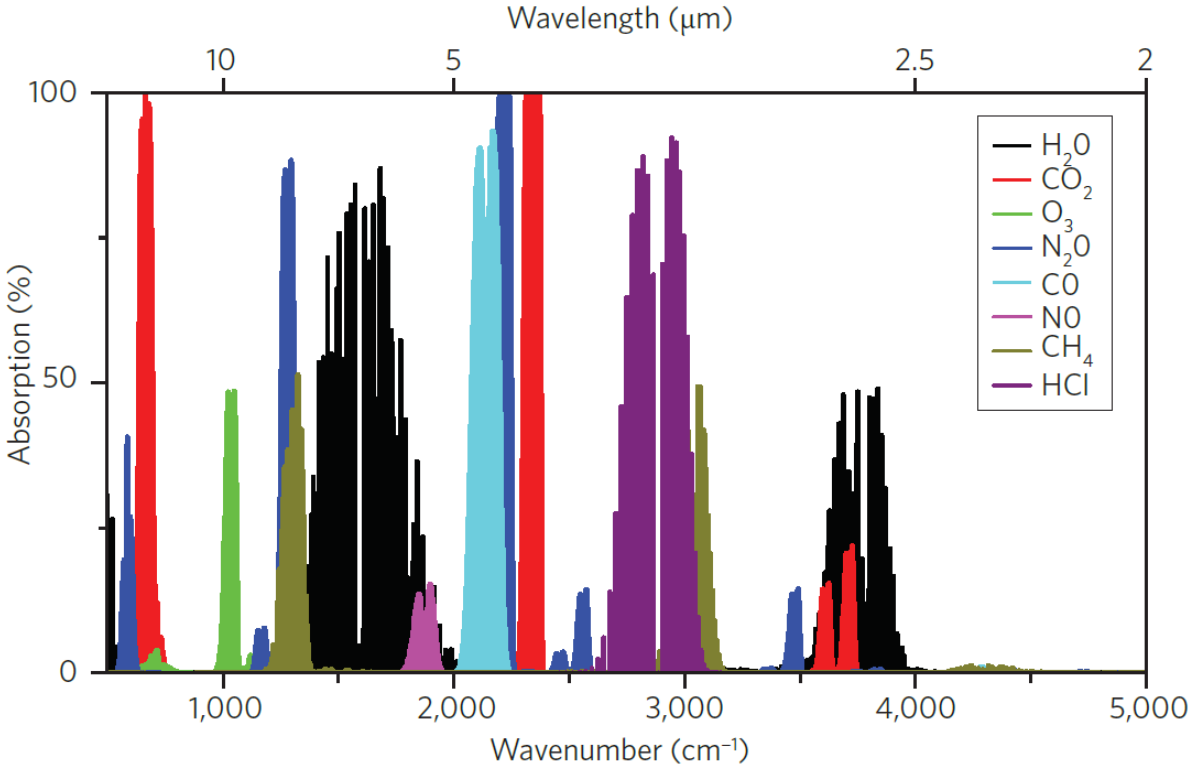

Figure 1.1: MIR absorption fingerprints of various gaseous molecules in the wavelength region of 2-20 μm for pressure of 133 Pa, temperature of 296.15 K and an absorption path length of 1 cm. The atmosphere transparency is mostly determined by H_2O and CO_2 absorption spectra. The raw data were taken from the 2008 edition of the HITRAN database [21]. The figure is taken from [22].

broad spectrum lamp and Michelson interferometer setup to produce an interferogram. By applying the Fourier transform (FT), the frequency spectrum can be reconstructed. The scanning procedure is in this case hidden inside the interferometer, which is shown in fig. 1.2.

It has a beam splitter, dividing the incident beam into two optical paths. Transmitted beam travels towards the moving mirror, reflects back and eventually reflects from the beam splitter to the detector. The reflected beam travels towards the fixed mirror, reflects back and transmits through the beamsplitter to the detector. By adjusting the position of the moving mirror, the optical path of the transmitted beam gets changed. The detector records the optical power of the interference spectrum between both beams and by changing the optical path of the transmitted beam an interferogram is recorded [25].

In order to determine the absorbance, a sample is mounted into the beam path, e.g. between interferometer and detector [25]. Interferogram is measured and spectrum gets calculated. Bear in mind, that the spectrum of a background (without the sample) should be always subtracted, because individual components like detectors and beamsplitters do not have a constant response for different wavelengths [25].

Overall, FTIR spectroscopy is nowadays one of the most successful spectrometric techniques used in many laboratories across the world, not only for the sample properties determination but also for the detector testing [26]. It records spectra over extended spectral spans in any region and exhibits quality and consistency [27]. The

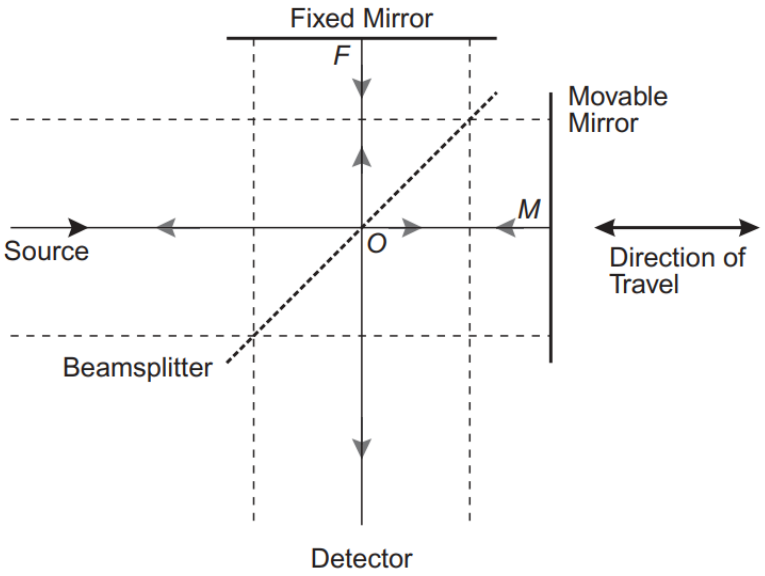

Figure 1.2: Michelson interferometer scheme. The median ray is shown by the solid line, whereas dashed line shows the extremes of the collimated beam. The figure is taken from [25].

most significant drawback of this technique is the moving mirror necessity, which increases the mechanical complexity [25] and limits the spectral resolution, which is inversely proportional to the maximum retardation of an interferometer [25]. For this sake, high-resolution instruments are usually very slow. A FTIR is also not suitable for high spatial resolution spectroscopy, which is often complementary method for microscopy. The reason is, the optical power per diffraction spot is limited for incoherent light sources [28].

Another popular technique for the measurements of MIR spectra is the Raman spectroscopy. It makes use of virtual energy levels, that occur naturally in molecules. A sample is illuminated with a monochromatic beam of radiation. Molecules in the ground electronic state can be lifted to the excited electronic state. As they fall back, they emit photons of the same energy. This is called the Rayleigh scattering and it is described as elastic process. Nevertheless, both the ground and the excited electronic states consist of many virtual states representing vibrational energies. If the molecule in the ground electronic and lower virtual state goes through the same electron absorption & photon emission process, but it ends in the higher virtual state, emission energy slightly decreases. This is called the Stokes scattering. In contrast, if this process results in a drop of the initially higher virtual state, emission energy slightly increases. This is called the anti-Stokes scattering. Together with Stokes scattering they contribute to the Raman scattering. Although, Raman scattering takes place in just one in 10^8 to 10^{10} transitions [25], it is enough to measure the scattered energy distribution and identify individual molecules.

Raman spectroscopy is a useful method, that is often found to be complementary to other techniques. Many bands, that are weak in the infrared spectrum are strong in the Raman spectrum and vice-versa [25]. What should not been overlooked is the fact, that the Raman spectrum has to be processed additionally by an interferometer [29] or by some dispersive technique, e.g. grating with the array of CCD detectors [30]. Although Raman spectroscopy suffered from relatively poor sensitivity before mid-1980s, it has

been significantly improved in the past decades [25]. Therefore, it became a widely used alternative to the spectrometers working directly in MIR spectrum. However, the disadvantage is low signal to noise ratio due to fluorescence of many molecules at the illumination energy, which effectively decreases the possible resolution [25].

Introduction of accurate tunable lasers in the MIR spectral region made it possible for direct scanning techniques. These techniques take advantage of the coherent illumination beam and are even reported to significantly surpass conventional FTIR in scanning speed, while maintaining the same figures-of-merit [28]. An external cavity QCL is exactly capable of that. The laser gain chip is placed inside a tunable external cavity. The typical tuning element is a diffraction grating. By mechanical rotation of the diffraction grating, the emission wavelength changes, resulting in a narrow band laser with a broad tuning range [28]. This technology is widely used in many laboratories although it requires precision optics and it is vulnerable to mechanical vibrations [31]. An alternative might be adapted sampled grating distributed feedback (DFB) laser, which combines two sampled grating sections within the same waveguide. The emission wavelength can be manipulated by changing the current density at one section relative to the other [31]. Thus, this device does not need any moving parts.

In conclusion, those techniques need either an interferometer setup, a disperser or a tunable narrow-band laser. This often leads to the moving part implementation, increasing the mechanical complexity and decreasing the resolution potential [27].

A solution, that might revolutionize the field of MIR spectroscopy, makes use of technology, that has been primarily developed for frequency metrology in the late 1990s [27]. Self-starting frequency combs, that can be generated in a QCL cavity [32], were suggested as illumination sources for many different spectrometers. They can either improve the resolution of conventional techniques [27] or they can be used for the implementation of new instruments, such as the dual comb spectroscopy [17]. This instrument does not suffer from necessity for moving parts and can potentially reach resolution equal to the comb line spacing [27] or even better in scanning mode [17]. Since this thesis is concerned with the MIR frequency combs generation, modulation and application, dual comb spectroscopy is going to be further studied at the end of this chapter.

1.2 Quantum cascade laser

QCLs are electrically pumped semiconductor lasers [33]. In contrast to the related Interband cascade laser (ICL)s and commonly used diode lasers, which utilize both electron and hole carriers, QCLs are unipolar. It means, only electrons in conduction band take part in energy transitions. They are confined in quantum wells, which are created by accurate growth of nanometer scale thin layers [34]. The barriers between the wells also consist of very thin layers, hence electrons can tunnel through. Individual wells are designed to form bigger elements, that correspond to the subbands in conduction band structure. Several quantum wells are organized in periods that repeat themselves in the QCL design. Typical designs consist of tens of periods [35]. The energy of the emitted light is determined by the overall design rather than energy of bandgap and electrons are not lost by the recombination with holes but directly recycled to the following cascade.

This section further continues with the fundamentals of QCLs, following with the

cavity design possibilities and an active region (AR) study.

1.2.1 Laser fundamentals

LASER is an acronym for the Light Amplification by Stimulated Emission of Radiation. According to the general literature, laser has to meet two conditions. The first is the population inversion of carriers and the second is the dominance of stimulated over spontaneous emission [1].

The population inversion can be described in a system with multiple energy states. The carrier population in thermal equilibrium naturally decreases by increasing the energy, which can be explained by Boltzmann distribution [1]. By achieving higher population at the upper energy state compared to the lower one, population inversion is created. If a single photon of energy equal to the energy difference between those levels passes through this system, emission of other photons will more likely occur rather than original photon absorption. In the emission mechanism, a photon is created by carrier relaxation from the upper to the lower state, which depletes the population inversion. In order to achieve and maintain the population inversion, a laser has to be artificially pumped usually by optical, electrical or chemical pumping [1]. Consequently, amplification of an EM wave can be achieved.

But how is the population inversion achieved in QCL and what is the emission mechanism? The answer lies in the voltage, that is applied across the device in the growth direction. The gradually changing electric potential modulates the natural potential of quantum wells causing a steady drift of electrons from negative to positive electrode. As electrons travel through, they eventually undergo radiative transitions which happen once per the cascade.

The energy transitions for a single cascade can be simplified as a two level system with a radiative transition between them and an additional ground state achievable by a non-radiative transition. The demand for an additional non-radiative transition originates from the fact, that population inversion cannot be achieved in the two level system only [1]. Simply because emitted light would get immediately absorbed by the opposite transition. Electrons from the ground state are further transported to the upper state of following period, completing the cycle. This system is illustrated in fig. 1.3.

The whole structure is pictured in the growth direction. Individual transitions are represented by the transition lifetimes between corresponding levels. Each transition is different, whereas upper to lower results in the emission of photon, lower to ground is essentially phonon related. The reason is, that the whole processes are controlled by the conservation of energy and momentum. The conservation of energy is rather straightforward (energy of emitted quasi-particle equals energy difference between individual states), momentum $\boldsymbol{p}$ cannot be arbitrarily chosen. Since momentum of photon is tiny compared to the electron momentum [37], we can say vertical transition τ_{32} can be supported by radiative transition. In comparison, the momentum mismatch for lower-ground transition τ_{21} is too high. Instead, electrons are mainly transferred with the help of LO-phonon scattering process [38]. In modern devices, those energy levels are specially designed to resonate with energies of LO-phonons [36] leading to significant decrease of transition lifetimes.

The second condition of the laser generation comes from an assumption, that the laser radiation is dominated by the stimulated emission. The stimulated emission

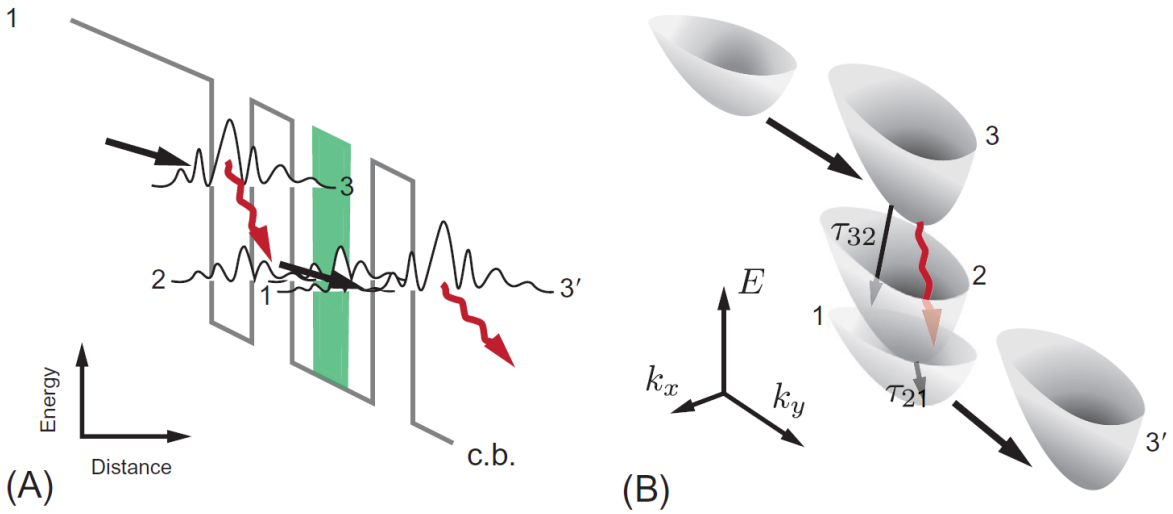

Figure 1.3: Schematic images of electron transport mechanism of QCL: (A) QCL diagram represented by energy versus growth direction and (B) a diagram in phase space. The parabolic envelopes represent energy distribution of the stationary energy states. Grey lines in (A) indicate potential energies of wells and barriers. Solid black arrows indicate electron transport. Wavy red arrows represent optical transitions for emission of photons. The figure is taken and modified from [36].

occurs, when an EM wave scatters a carrier from the upper to lower level and photon is emitted. Emitted light is coherent because it travels in the same direction as the original wave. It has the same energy and is in phase with original EM wave [1]. Spontaneous emission is on the other hand an incoherent process. The electric amplitude E does not change the probability of transition and individual photons are randomly phase related to each other [39]. In the next step, we are going to neglect the contribution of spontaneous emission, as it is not directly related to the generation of frequency comb. Instead, spontaneous emission will be added later on in a form of random number generator to the simulation software.

The whole dynamics of the system, that supports both stimulated emission and non-radiative transitions can be expressed by coupled two-level density matrix equations 1.2 - 1.5 from [40] and [41]:

$$\frac{\partial n_u}{\partial t} = J - \frac{n_u}{T_{ul}} + \frac{n_u}{T_{ug}} - i\frac{\mu E}{\hbar}(\rho_{ul} - \rho_{lu}) + D\frac{\partial^2 n_u}{\partial z^2}, \tag{1.2}$$

$$\frac{\partial n_l}{\partial t} = \frac{n_u}{T_{ul}} - \frac{n_l}{T_{lg}} + i\frac{\mu E}{\hbar}(\rho_{ul} - \rho_{lu}) + D\frac{\partial^2 n_l}{\partial z^2}, \tag{1.3}$$

$$\frac{\partial n_g}{\partial t} = \frac{n_u}{T_{ug}} + \frac{n_l}{T_{lg}} - J + D\frac{\partial^2 n_g}{\partial z^2}, \tag{1.4}$$

$$\frac{\partial \rho_{lu}}{\partial t} = (i\omega_0 - \frac{1}{T_2})\rho_{lu} + i\frac{\mu E}{\hbar}(n_u - n_l), \tag{1.5}$$

where u represents the upper level, l lower and g additional ground level. T_{ul}, T_{ug} and T_{lg} represent non-radiative transition lifetimes, that are indirectly proportional to the non-radiative transition probabilities, diagonal terms of the density matrix ρ_{uu}, ρ_{ll}

are relabeled to more diagrammatic form n_u, n_l. Together with n_g they represent sheet densities of electron populations in the upper, lower and ground state. J represents the pumping current to the upper level originating from applied voltage. ω_0 stands for transition frequency and D for spatial carrier diffusion.

ρ_{ul} and ρ_{lu} represent the off-diagonal density matrix elements. From the definition of dipole moment $< p(t) >_{av} = \rho_{lu}\mu_{ul} + c.c.$ [41], ρ_{lu} can be called normalized dipole moment μ. ρ_{lu} can be directly determined from eq. 1.5. Since all Hermitian matrices (including the density matrix) hold, that one off-diagonal element can be directly determined from the complex conjugate of corresponding off-diagonal element [42], $\rho_{ul} = \rho^*_{lu}$. Hence, eq. 1.5 can be rewritten for ρ_{ul} just by flipping $\pm$ signs for all imaginary parts.

The first term on the right side of eq. 1.5 $\propto \rho_{lu}$ comes from the time independent Hamiltonian [41], that is extended by a dephasing process $\propto 1/T_2$. The origin of polarization dephasing term T_2 comes from the non-radiative scattering processes, that destroy the coherent superposition between two states, broadening the transition energy responsible for additional losses of temporal coherence [43]. The dephasing time has two significant contributions: First originates from the limited lifetimes of the lower and upper level and other from elastic scattering such as interface roughness and alloy scattering [44]. The second term on the right side of eq. 1.5 stands for the time perturbation of the Hamiltonian. Time dependent term $n_u - n_l$ represents the population inversion. It has a huge impact on ρ_{lu}, and ρ_{ul}. If population inversion is achieved by $n_u > n_l$, terms in eq. 1.2, 1.3 $\propto \rho_{ul} - \rho_{lu}$ stand for the stimulated emission. In some notations [19], $\rho_{ul} - \rho_{lu}$ is replaced by $-2i\,\mathrm{Im}(\rho_{ul})$. By substituting those values into eq. 1.2, 1.3, we can see that both equations are strictly real. If $n_u < n_l$, $\rho_{ul} - \rho_{lu}$ represents opposite process called light absorption.

The whole set of equations is completed by EM wave equation extended by term from the two-level density matrix description [40]:

$$\frac{\partial^2 E}{\partial z^2} - \frac{n^2}{c^2}\frac{\partial^2 E}{\partial t^2} = \frac{\Gamma\mu}{\varepsilon_0 c^2 L_p}\frac{\partial^2(\rho_{ul} + \rho_{lu})}{\partial t^2}, \tag{1.6}$$

where Γ is the confinement factor, that determines the power ratio within the gain environment to the overall power and L_p is the thickness of single cascade. Term $\rho_{ul} + \rho_{lu}$ can be rewritten to $-2\,\mathrm{Re}(\rho_{ul})$.

In following steps, previously defined equations are going to be adjusted and simplified for better understanding of physical processes. First, we add eq. 1.2-1.4 together. For $n_{tot} = n_u + n_l + n_g$ equations are simplified:

$$\frac{\partial n_{tot}}{\partial t} = D\frac{\partial^2 n_{tot}}{\partial z^2}, \tag{1.7}$$

where all internal exchanges cancel out with each other. According to eq. 1.7, the overall concentration of electrons can still change in space and time. However, because of the conservation of total number of electrons $\delta(\int_{-\infty}^{\infty}(n_{tot}dz)) = 0$, diffusion cannot be arbitrarily determined.

Simply for demonstration purpose, populations n_u, n_l and n_g can be considered constant in time. This should illustrate steady state and clarify roles of both emission mechanisms. In addition we can integrate eq. 1.2 - 1.4 in space to get rid of alternating diffusion function and obtain:

$$\begin{aligned} J &= sc_{ul} + sc_{ug} + st_{ul}, \\ sc_{ul} + st_{ul} &= sc_{lg}, \\ sc_{ug} + sc_{lg} &= J, \end{aligned} \tag{1.8}$$

where sc_{ij} represents the non-radiant transition from state i to j and st_{ij} the stimulated emission. All equations show the conservation of carriers. The first line presents the action of current pumping on transition mechanism. Contributions of the electric field dependent st_{ul} can be increased by higher electric field, so that more current goes into the stimulated emission mechanism. The last line shows the importance of the lower-ground carrier extraction. Since $sc_{lg} \gg sc_{ug}$, whole current has to be supported by this non-radiant transition, putting pressure upon phonon-resonant engineering.

To achieve sufficient light amplification, an optical feedback should be introduced, which forces the EM wave to travel through the gain media multiple times. This can be fulfilled by locking the gain media in some kind of cavity, inside which EM field changes periodically, while only part of the energy escapes at each round-trip [1].

1.2.2 Laser cavity

There are a few ways how to achieve optical feedback. The most fundamental is certainly the Fabry-Perot cavity design. It consists of two parallel reflective surfaces sandwiching the gain media between themselves. The gain media in QCLs has been already discussed, but where and in which form are those reflective surfaces located? Across different laser types, dielectric coatings are used the most [45]. They are directly deposited on the facets of solid state gain medium [45] or at the ends of the tube of gaseous gain medium [46]. Although dielectric coatings are also used for the short cavity QCLs to increase the wall plug efficiency, most of the QCL devices make do with bare facets. The reason is, high refractive index of used semiconductors at the interface with the low refractive index of low concentration gas or vacuum form a partially reflective surface, that is due to relatively high gain efficient enough for most devices [36, 14, 24]. This thesis considers self-starting lasers. It means, studied QCLs get initially pumped creating the population inversion. Due to the spontaneous emission, the first photons are created. They further stimulate electrons in the upper level. By this process, an EM wave is formed. If pumping current exceeds the threshold value J_{th}, wave travels between both reflective facets and increases in intensity at every round-trip.

Next, intensity and power at a certain point in the cavity will be studied in respect to the round-trips. As the intensity of light increases, the relative contribution of stimulated emission increases too, while population in upper state decreases. Since pumping current can support only limited number of electron transitions, the system eventually reaches the gain saturation [1], where gain saturation, saturation intensity E_{sat} and saturation power P_{sat} are defined by the system constants, that specify the intensity and power of optical transparency. Power starts to drop due to the overall cavity losses. After the few alternations stabilized power in respect to round-trips is reached. This takes tens to hundreds of round-trips, depending on the cavity design and applied current. Eventually, the overall losses are perfectly balanced by gain of the material.

After reaching this state, slight and often unrecognizable fluctuations of overall intensity occur in respect to additional round-trips. Because of that, the system has not reached the stabilized state yet. Initially photons with a random phase relation, originating from multiple spontaneously emitted photons form incoherent optical output. If a self-starting FM laser is designed correctly, phases of photons of different energies couple with each other forming the frequency comb. The laser is now in a steady state, it is phase-locked and frequency spectrum correlates with spectra of few previous round-trips. This process takes thousands of round-trips. In comparison to reaching state of gain balance, it does not have to converge at all [18] depending on device parameters [4]. In some cases, photons cannot overcome initially randomly phase distribution or they reach state, where some overall phase dependence can be observed, but a considerable number of photons of different energies cannot couple with others. Optical output of this device is an incoherent multi-mode spectrum [3]. It does not correlate with spectra of previous round-trips and we could even say, such a device cannot reach steady state at all. Although this declaration seems right, in literature, steady state refers to the condition, where constant power has been reached and gain balances out the losses of cavity [1].

In previous paragraphs, optical gain has been vaguely mentioned several times. As it is one of the most fundamental figure-of-merit in laser technology, it will be explained in the following lines. The gain is defined as the derivative of the logarithm of power as it passes through the medium [47]. It can be expressed in a form:

$$g = \frac{dP/dz}{P}, \tag{1.9}$$

where z is the direction of travelling wave. Since gain can be expressed differently in other literature, it is important to stick to the definition and not to confuse it with the power amplification factor, since power amplification is $\propto exp(g)$ [39]. As waveguide losses can be represented by similar term called intensity loss coefficient α_w and power attenuation is $\propto exp(-\alpha_w)$, it can be used to represent gain at the threshold, which is determined exclusively by cavity losses. Gain threshold for Fabry-Perot cavity is defined in eq. 1.10:

$$g_{th} = \alpha_w - \frac{1}{2L} ln(R_1 R_2), \tag{1.10}$$

where L is the length of the cavity, R_1 is the reflectance of left facet and R_2 reflectance of right facet. For this case, α_w is considered to be constant. This assumption does not have to stay valid for high optical powers, where attenuation decreases with increase of optical intensity due to the absorber saturation. This phenomenon is successfully used for phase-locking of ICLs [48, 49].

Other important terms are unsaturated and saturated intensity gain. They connect gain directly with the emission mechanisms. First, we define T_1 as following:

$$T_1 = \left(\frac{1}{T_{ul}} + \frac{1}{T_{ug}}\right)^{-1}. \tag{1.11}$$

Unsaturated gain is according to derivations in [19] expressed in form:

$$g_0 = \frac{\Gamma \mu^2 \omega_0 T_1 T_2 J}{\hbar n \varepsilon_0 L_p}. \tag{1.12}$$

At low electric intensity $g \simeq g_0$, therefore g_0 is sometimes referred as the small signal gain [50]. It is independent on the electric intensity and $\propto J$. Since g_{th} is independent on applied current, g_0/g_{th} is used in the travelling wave model (TWM) to determine the ratio of applied to the threshold current. If $g_0/g_{th} \geq 1$, the current threshold is surpassed and laser can be studied. For higher values of optical intensity, gain can be represented by saturated intensity gain. This is expressed in eq. 1.13

$$g(P) = \frac{g_0}{1 + \frac{|E_+|^2 + |E_-|^2}{E_{sat}^2}} = \frac{g_0}{1 + \frac{P}{P_{sat}}}. \tag{1.13}$$

We have already described the effect of the optical feedback on the gain material and discussed gain. Now, it is time to mathematically describe the whole system with use of the derivation from the previous section. For this sake, the general formalism of sheet densities of electron population from eq. 1.2 - 1.5 and electric amplitude E from eq. 1.6 will be extended to support most essential cavity contributions. In cavity EM waves travel in both directions, where E_+ represents the slowly varying envelope of the right propagating wave and E_- the slowly varying envelope of the left propagating wave. These waves interfere with each other forming the standing wave interference pattern. This can be observed in fig. 1.4.

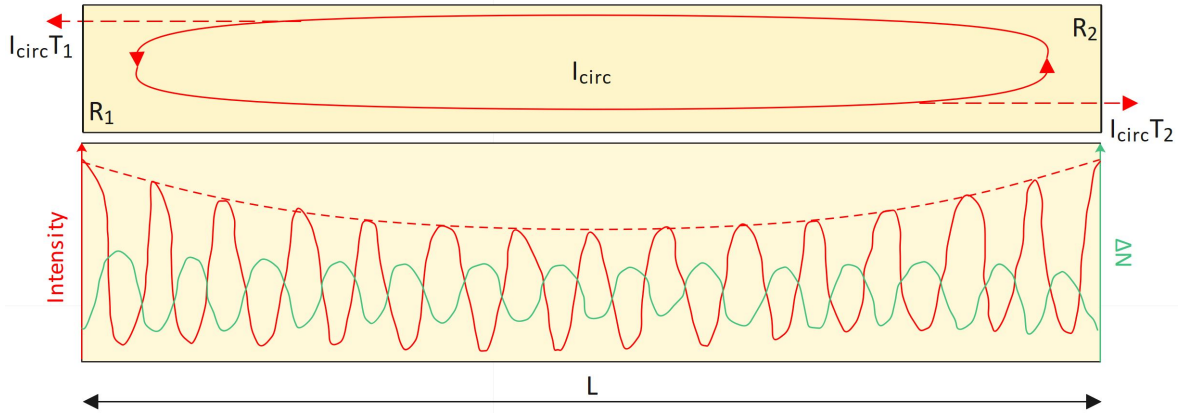

Figure 1.4: Schematic image of the Fabry-Perot cavity of length L. Gain material is localized between two semi-reflective mirrors of reflectance R_1 and R_2. Circulating EM wave is represented by electric intensity $I_{circ} = |E_{circ}|^2$ inside the cavity, while part of the intensity $I_{circ}T_i$ exits at each mirror. Interference pattern of right and left propagating wave is created. The red solid line in figure below represents the space-dependent electric intensity, red dashed line intensity of envelope and green solid line shows the population inversion $\Delta N = (n_u - n_l)N$, where N is the spatial concentration of electrons [41].

The alternating electric intensity causes alternating gain. Since gain saturation increases with optical intensity, the gain reaches its maximum at the minimum value of intensity and vice-versa. The effect, when intensity antinode (maximum) locally depletes the population inversion is called the spatial hole burning (SHB) and it has various consequences on laser operation. In lasers, SHB has significant impact on comb generation. It has been numerically proven [19], that inclusion of this term significantly increases number of modes compared to the case without SHB term. In contribution with fast gain dynamics, that applies in general to QCLs, it causes almost constant intensities of individual modes in frequency domain [32]. SHB effect is so significant, that

it is necessary for FM comb generation [19][32]. Mathematically speaking, the whole term is introduced through additional grating components n_{u0}, n_{l0} and n_{g0}. Those are added to the sheet densities of individual energy levels [19]. Previously discussed effects of cavity are summed up in set of eq. 1.14:

$$\begin{aligned}
E(z,t) &= \frac{1}{2}[E_+(z,t)e^{i(\omega_0 t - k_0 z)} + E_-(z,t)e^{i(\omega_0 t + k_0 z)} + c.c.],\\
n_u(z,t) &= n_{u0} + n_{u2}e^{-2ik_0 z} + n_{u2}^* e^{2ik_0 z},\\
n_l(z,t) &= n_{l0} + n_{l2}e^{-2ik_0 z} + n_{l2}^* e^{2ik_0 z},\\
n_g(z,t) &= n_{g0} + n_{g2}e^{-2ik_0 z} + n_{g2}^* e^{2ik_0 z},\\
\sigma_{lu}(z,t) &= \eta_+ e^{-i(\omega_0 t - k_0 z)} + \eta_- e^{-i(\omega_0 t + k_0 z)},
\end{aligned} \tag{1.14}$$

where $k_0 = n\omega_0/c$ and $c.c.$ is the complex conjugate. As has been highlighted in eq 1.2 - 1.4, injection current can be divided into individual contributions. Since those contributions obey set of eq. 1.11 inside cavity, current J should be changed correspondingly [40]. This is shown in eq. 1.15:

$$J(z,t) = J_0 + J_2 e^{2ik_0 z} + J_2^* e^{-2ik_0 z} \tag{1.15}$$

By substituting eq. 1.11 and 1.12 into eq. 1.2 - 1.5 with an addition of waveguide losses α_w into envelope functions, we obtain complete set of coupled density matrix and Maxwell equations [19], as it is used in [40]:

$$\begin{aligned}
\frac{\partial n_{g0}}{\partial t} &= \frac{n_{u0}}{T_{ug}} + \frac{n_{l0}}{T_{lg}} - J_0,\\
\frac{\partial n_{g2}}{\partial t} &= \frac{n_{u2}}{T_{ug}} + \frac{n_{l2}}{T_{lg}} - J_2 - 4k^2 D n_{g2},\\
\frac{\partial n_{u0}}{\partial t} &= J_0 - \frac{n_{u0}}{T_{ul}} - \frac{n_{n0}}{T_{ug}} + i\frac{\mu}{2\hbar}[E_+\eta_+^* + E_-\eta_-^* - c.c.],\\
\frac{\partial n_{u2}}{\partial t} &= J_2 - \frac{n_{u2}}{T_{ul}} - \frac{n_{u2}}{T_{ug}} - 4k^2 D n_{u2} + i\frac{\mu}{2\hbar}[E_+\eta_-^* + E_-^*\eta_+],\\
\frac{\partial n_{l0}}{\partial t} &= \frac{n_{u0}}{T_{ul}} - \frac{n_{l0}}{T_{lg}} - i\frac{\mu}{2\hbar}[E_+\eta_+^* + E_-\eta_-^* - c.c.],\\
\frac{\partial n_{l2}}{\partial t} &= \frac{n_{u2}}{T_{ul}} - \frac{n_{l2}}{T_{ug}} - 4k^2 D n_{l2} - i\frac{\mu}{2\hbar}[E_+\eta_-^* - E_-^*\eta_+],\\
\frac{\partial \eta_+}{\partial t} &= -i\frac{\mu}{2\hbar}[(n_{u0} - n_{l0})E_+ + (n_{u2} - n_{l2})E_-] - \frac{\eta_+}{T_2},\\
\frac{\partial \eta_-}{\partial t} &= -i\frac{\mu}{2\hbar}[(n_{u0} - n_{l0})E_- + (n_{u2}^* - n_{l2}^*)E_+] - \frac{\eta_-}{T_2},\\
(\frac{n}{c}\frac{\partial}{\partial t} + \frac{\partial}{\partial z})E_+ &= i\frac{\Gamma\mu\omega_0}{n\varepsilon_0 c L_p}\eta_+ - \alpha_w E_+,\\
(\frac{n}{c}\frac{\partial}{\partial t} - \frac{\partial}{\partial z})E_- &= i\frac{\Gamma\mu\omega_0}{n\varepsilon_0 c L_p}\eta_- - \alpha_w E_-.
\end{aligned} \tag{1.16}$$

These coupled differential spatio-temporal equations are often called Maxwell-Bloch equations and they fully determine laser generation for system with 2 energy states and an additional ground state in the form of slowly varying envelopes [40].

Cavity effects that influence these equations have been demonstrated on a Fabry-Perot cavity. It has been done for illustrative purposes and also because Fabry-Perot cavity will be calculated in the simulation chapter. Since any step used for derivation of Maxwell-Bloch equations did not require the Fabry-Perot cavity, eq. 1.16 can be applied to any kind of optical feedback.

Alternative cavity design for QCLs uses ring resonator. In this type of cavity, light can circulate in two opposite modes, clockwise and counterclockwise. In respect to the emission mechanism, there is one significant difference to the Fabry-Perot cavity. Innately only one propagation component occurs. As a result, SHB is expected to be negligible [51]. Even though SHB should prevent QCL rings to form frequency combs at currents near the threshold, existence of frequency combs has been experimentally confirmed [52]. Current focus points toward simulations of nonlinear processes, that should be responsible for this interesting result [52]. Although TWM possesses also ring cavity functionality the merit of this thesis heads toward Fabry-Perot cavities, thus Fabry-Perot design is going to be used in following sections exclusively.

1.2.3 Active region

In this study, AR denotes the active region of laser. According to the definition, AR could be described as the particular region of radiative electron transition inside each cascade [36] or as the whole set of cascades [53]. In this thesis, second definition is used. The number of cascades is carefully designed for optimal performance. This value was already claimed to be in range of units to tens. In general, devices producing high power optical output [16] consist of a large number of cascades, while devices with emphasis on high wallplug efficiency and single transverse mode application consist of fewer cascades [35].

In the beginning of this chapter, basic introduction to emission mechanism of QCLs has been presented, mostly to justify used models. Yet, a detailed study of AR has not been delivered, especially study of non-radiative transitions. In order to describe gain mechanisms in the AR, band simulations are used. By modelling electric potential in direction of growth, probability density of electrons can be calculated. Results are plotted in spatial dependent energy diagram, as we can see in fig. 1.5

The following paragraph analyses this diagram from [53] from left to right. Potential distribution across the cascade is tilted due to applied voltage. Electrons radiatively from subband to subband in gain section. In this particular device electrons are further horizontally and vertically extracted to the injection section. The horizontal extractor creates potential barrier confining electrons in the upper state of the gain section. The vertical extractor significantly reduces thermal backfilling of electrons from the high energy states in the injector. In this case, the extraction is performed through scattering assisted tunnelling [53]. Commonly QCLs use vertical extraction via an LO-phonon stair instead [38]. At the end of vertical extractor doping levels of semiconductors are increased. This results in band bending [36]. Doping levels stay high for first part of the injector section, decreasing to usual values in second part. Eventually, high probability density of electrons is achieved in narrow wells and electrons enter next cascade.

After detailed study of different sections of AR, it became evident, there are enor-

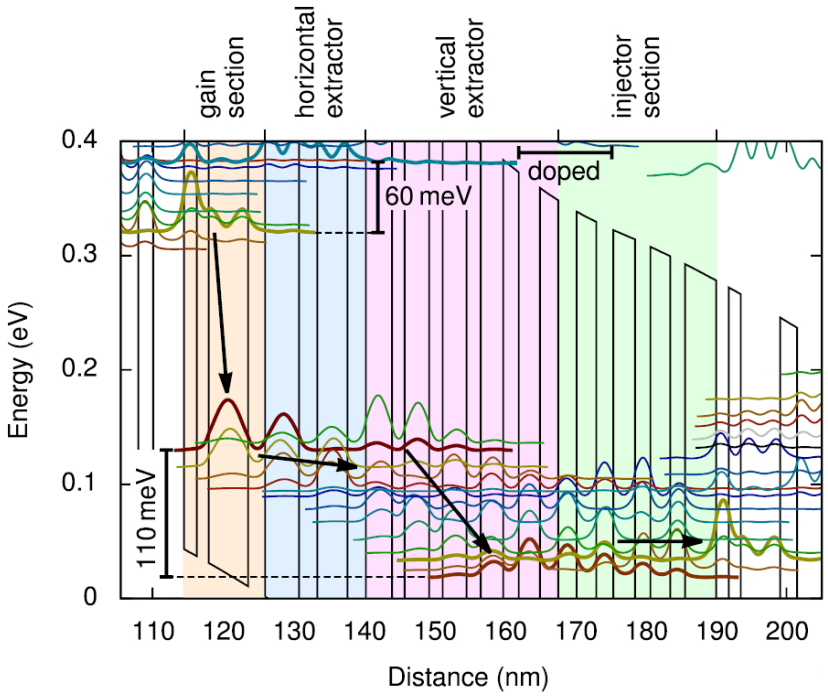

Figure 1.5: Band diagram of bi-functional Quantum cascade laser and detector (QCLD) in laser operation at maximal wallplug efficiency. Potential of wells and barriers is graphically represented by narrow black lines. Colored lines express probability density of electrons at given energy state. Black arrows show expected direction of transition of electrons. Background colour separate individual regions according to their role. Figure is taken from [53] and modified.

mous demands for fabrication quality of individual layers. Layers are so thin, that they consist of few number of atoms. Even small thickness deviation of wells changes probability density of electrons and thickness deviation of barriers significantly influences tunneling rates. In addition rough interfaces can support unwanted non-radiative relaxations [38]. Luckily, accurate growing techniques such as molecular beam epitaxy [54] and metal-organic vapor-phase epitaxy [55] show precise, reproducible results of growth in respect to QCL application.

Materials of individual layers cannot be arbitrarily chosen. They consist of lattice matched compounds, that support conduction band engineering of wells and barriers. It turns out, lattice matching of different compounds is especially challenging and used substrate limits growth to very few materials. In conclusion III-V semiconductors are usually used, e.g. InP substrate, that supports InP wells and $In_{0.52}Al_{0.48}As$ barriers with addition of $In_{0.53}Ga_{0.47}As$ outside of AR [16].

1.2.4 Overall design

In this section overall 3D design of QCL with Fabry-Perot cavity is discussed. We start with the most obvious dimension. It is the direction of wave propagation, which has been already denoted by the length of cavity L. Other two dimensions are more complex because of the electron transport, heat transport, waveguiding properties and applied current in the growth direction, resp. heat transport and waveguiding properties in the lateral direction. This thesis is not concerned with heat or electron transport

outside of AR, thus interested reader is referenced to external source [56].

The most fundamental design of Fabry-Perot QCL is the ridge architecture, which is shown in fig. 1.6.

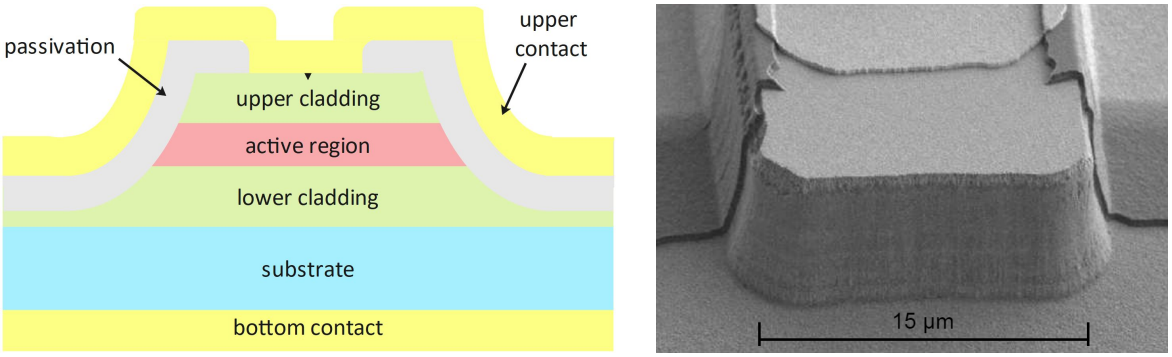

Figure 1.6: Scheme on the left illustrates ridge cross-section. On the right side there is an image from electron microscopy. Right image is taken from [24] and modified.

According to the left part of fig. 1.6, whole structure is sandwiched between electrically contacting layers, usually from Au with some thin layer of adhesion metal. They serve as conductive layers, where the applied voltage is introduced. Since the substrate has usually relatively high doping levels, which would increase overall losses of propagating wave, the AR is separated from bellow by a thick, low doping and low refractive index cladding layer. This layer is also located above AR to avoid losses with the metallic interface. Most lasers have an additional separate-confinement layer (SCL) (missing in scheme) between AR and cladding layers, where SCL has high refractive index and low doping level. Hence, it helps to confine light to the environment of minimal losses. The whole ridge is laterally protected from the upper contacting layer by passivation. This simplified scheme is not intended for dimension scaling. For those purposes serves the image on the right.

The whole structure is fabricated in set of steps. First, layers up to the upper cladding are grown on the top of a cleaned substrate inside the growth chamber. Next, laser, that is defined by length of the cavity and width of the ridge is selectively covered by thick layer of SiN, which can be achieved due to optical lithography. Further, uncovered spots are etched out to selected depth. This can be done by dry or wet-etching. For anisotropic dry-etching case, the ridge is rectangular-like in growth to lateral dimension. Isotropic wet-etching results in a ridge from the left scheme in fig. 1.6. As soon as a protective SiN layer is removed, the whole structure is covered by SiN again except the top of the ridge, which is directly covered by contacting layer, which is also applied from the bottom of the substrate. In the last step, the whole structure is mounted on the chip.

1.3 Frequency combs

According to eq. 1.2 - 1.6, EM waves would travel at a single frequency $f_0 = \omega_0/(2\pi)$. Introduction of optical feedback in set of eq. 1.14, causes periodically changing sheet densities of individual populations across the cavity. More importantly, this effect is carried forward to the normalized dipole moment ρ_{lu}, which has enormous impact on the frequency of the emitted light. By analyzing the mode-locked spectrum inside the

cavity, we could determine finite set of frequencies, that could represent the entire signal. They denote longitudinal modes and can be extracted from the solution of Maxwell-Bloch equations.

Luckilly, the position of individual peaks in frequency domain can be also obtained from much easier and more intuitive model. For each longitudinal mode travelling waves preserve phase after one roundtrip at any point in the resonator. Periodically changing signal $E \propto sin(kz)$ can be expressed at any point as $sin(\varphi) = sin(2kL + \varphi)$. Hence, solution for wavevector k can be expressed as:

$$k_m = \frac{2L}{m}, \tag{1.17}$$

where m can be represented by any natural number. From dispersion relation of light $f_m = k_m c/(2\pi n)$, we can rewrite eq. 1.17 into form:

$$f_m = \frac{mc}{2nL}. \tag{1.18}$$

The frequency difference between two closest modes can be expressed as $f_{rep} = f_{m+1} - f_m$. This is shown in eq. 1.19:

$$f_{rep} = \frac{c}{2nL}. \tag{1.19}$$

Following the last equation, we can see, f_{rep} is defined just by the effective index of cavity medium and length of the cavity, which is the same relation as the roundtrip frequency in TWM. As it is obtained for general case of any two closest modes, it is safe to say, all modes are equidistant in frequency space. For this sake, we can define positions of individual modes in form commonly used in frequency combs studies:

$$f_m = f_0 + m f_{rep} \tag{1.20}$$

where f_0 is the carrier offset frequency and f_{rep} repetition frequency (also referenced as a comb tooth spacing). This expression finally reveals the term comb. Individual modes form narrow peaks that resemble comb teeth. Just by using this simple derivation, we determined possible positions of all frequency peaks. This model defines infinite number of frequencies, which is physically incorrect, because the gain is in general frequency dependent and does not have infinite bandwidth. Hence, only limited number of modes will be found. Therefore m is restricted to the number of modes.

The differences between frequency comb and multimode regime can be more clearly demonstrated on phase relation between individual modes. Amplitudes and phases of peaks in frequency spectrum cannot be determined by such intuitive model as their position. Therefore, TWM model is used for simulations of generation of frequency combs.

If we assume multi-mode spectra as a common case for laser cavities, we can introduce some techniques, that can overcome chaos and generate frequency combs. The most important aspect of this study is the self-starting comb generation.

1.3.1 Self-starting comb

As has been explained in eq. 1.14. Model with counterpropagating waves has to be supplemented with a grating component representing action of SHB. If we assume two counterpropagating waves at different frequencies, grating components would beat

at frequency Δf, that would lead into energy transfer not only between those two modes, but any modes within the same beating Δf. Since intersubband transitions feature in general strong third-order optical nonlinearities [8], we can represent this effect on refractive index $n(\omega) = n_0(\omega) + n_{nl}(\omega)$, where n_{nl} represents contribution of different nonlinearities, e.g. linewidth enhancement, Kerr effect and GVD. Since refractive index determines the phase velocity of wave $v(\omega) = c/n(\omega)$, Travelling waves of different frequencies would modulate themselves according to their phase mismatches caused by $n(\omega)$ [57].

The nonlinear effect of saturable absorption $\alpha_w(E)$, that is used to generate frequency combs in ICLs [49] leads to the generation of amplitude modulated combs. In amplitude modulation, all beatnotes from neighboring modes are equal in phase, forming one strong beatnote in the frequency domain. As a result, a signal of periodically repeating pulses is generated [58].

In QCLs, fast gain dynamics leads to efficient four-wave mixing [58], which is the process where three waves of different frequencies produce a fourth wave [57]. four-wave mixing mechanism depends on intermodal beatings between original frequencies [57]. Such system can be described as frequency modulated. In FM comb, phases are splayed uniformly across the unit circle and signal is generated in CW form [58].

FM enables QCLs to generate self-starting frequency combs, which has been first confirmed in 2012 by the group of prof. Faist at ETH Zurich [8]. Ever since that, frequency combs found many different applications in the QCL field. Since the four-wave mixing has not been fully theoretically described yet, forecasting of future measurements are being done mainly with help of simulations. Simulations of passive mode-locking will be part of the simulation chapter.

1.3.2 Injection locking

Injection locking describes mixing of external signal with the signal in the cavity in order to lock original comb to the external source. Although external signals can be used for mode-locking of otherwise multimode lasers [39], this work presents action of external signal upon already mode-locked comb in order to control the repetition frequency. The beatings between any two neighboring modes in a frequency comb can be represented by a set of coupled oscillators. In general, one of these oscillators or complete set can be locked in frequency and phase to external oscillator, if individual oscillators exhibit enough coupling with each other [59]. Modulation is successful, when original set collectively couples to the external oscillator and the whole system stays in mode-locked state.

There are two relevant injection locking techniques for QCLs. First uses a radio-frequency electric signal, that is applied to the cavity. It is called electric injection locking.

Studied lasers emit at $\lambda = 8\ \mu$m, that corresponds to $f \approx 37$ THz. Such a frequency obviously cannot be achieved in electric circuit, thus applied signal cannot directly modulate individual comb teeth. Instead, signal is tuned to be close to the roundtrip frequency f_{rep}, leading to the modulation of the beating. In the case of applying an electric signal to the short section at one facet, where the electrical beating is most susceptible to the injected signal [60], all teeth can be coherently locked to an external signal [61]. In conclusion, this technique can be used to modulate beatnote frequency f_{rep} and may lead to future miniaturization of dual-comb spectrometers [61].

Other relevant technique is the optical injection locking. It is based on the interaction of an external light source with the EM signal inside the cavity [39]. In our case, the external light source is represented by a DFB grating, that provides an additional optical feedback via backward Bragg scattering from a periodic perturbation of refractive index [62]. In the QCL ridge architecture, sufficient DFB gratings have been demonstrated via lateral double-sided grating, that has been fabricated by conventional photolithography [63]. DFB structures enable single mode narrow band emission, which is the main reason for their implementation. Singe frequency signal of DFB can be expressed in a simple form:

$$E_{DFB}(t) = E_0 e^{i\omega_o t}, \tag{1.21}$$

where E_0 represents the amplitude of the electric intensity and ω_o central frequency of the DFB laser. ω_d will be on the other hand referenced as the detuning frequency, which is the difference between frequency of selected mode and ω_o. This signal is directly applied to one of the facets. Bear in mind, the actual amplitude of the DFB laser should be increased by the factor of Fresnel coefficient to account for the finite transmittance of the facet.

Since the DFB laser impacts frequency distribution inside the cavity, whereas cavity signal does not have any influence on the frequency of DFB laser, the DFB laser is often referenced as the 'master' laser and cavity is called the 'slave' [64]. The main purpose introducing the master laser is to directly modulate the frequency of a selected mode. The amplitude of the injected signal is usually low relative to the power inside the cavity to prevent chaotic behaviour. The frequency usually differs from the frequency of selected mode by units of tens of MHz, which is in our case approximately 3 orders of magnitude less compared to the f_{rep}. The master laser is expected to completely capture the selected mode [64] or pull it towards itself [59]. For a second case we expect besides the original and the injected peak additional peaks generated by the interference of those spectra. In all cases, shifted frequency of the selected mode applies to other modes equally, preserving original f_{rep} [17], which is the most significant difference to the electric injection locking. As a result those techniques are meant to be complementary rather than directly concurrent.

Figure 1.7: Scheme of different operations of optical injection locking. a) shows the set of optical injection locked states starting from the passive mode-locked simulation, b) shows the progressive regime, where each injection locked state serves for injection locking of following frequency.

Optical injection can be put into practice in two ways. This is illustrated in fig. 1.7.

Simulation of case a) presents the set of steady states for each frequency. Case b) simulates system in time evolution, when frequency changes gradually. The advantage of the first operation is relative simple interpretation of results. Other operation should benefit from larger locking window. Furthermore, it should simulate more trustworthy possible experiment.

1.3.3 Dual comb spectroscopy

At the end of the Spectroscopic methods section, comb spectroscopy has been introduced promising new technique with vast potential in MIR region. Leaving the implementations of frequency combs into conventional spectrometers aside, dual comb spectroscopy is the most exciting novel technique for accurate and fast spectral measurements [27] and the most promising application of research in the field of optical injection locking of QCLs.

Dual comb spectroscopy works on the principle of a multi-heterodyne beat detection [17]. The signal from the first comb travels through the gas cell with a sample and gets mixed with the signal of local oscillator, which is the second comb of slightly different line spacing f_{rep}. Resulting interferogram can be translated by the FT to the beatnote spectrum. Because of different line spacing between both combs, each pair of corresponding frequencies generates different beatnote. According to this, individual beatnotes can be reversely translated to the frequency domain and intensity of each mode can be measured. Based on that, sample transmission can be determined up to the resolution of line spacing of the first comb [27].

If we apply this to a few cm long QCL cavity, the resolution would reach units to tens of GHz, which is better or similar to the resolution of conventional FTIR spectrometers, but still insufficient for small liquid molecule analysis and gas sensing [17]. By shifting the offset frequencies of both the sample comb and the local oscillator, we introduce a frequency scanning recording high number of points in detuning range up to f_{rep}. Eventually, a resolution of f_{rep} divided by the number of scanning steps (but not better than the width of an individual mode peak) can be reached. This resolution enhancement within the dual comb spectrometer is pictured in fig. 1.8.

In the case of a QCL cavity, enhanced resolution could reach few MHz and total acquisition time could reach tens to hundreds of ms. Still, there are multiple factors, that could massively degrade the functionality of the whole device, such as insufficient injection locking, comb instabilities or low temporal coherence.

In conclusion, dual comb spectroscopy is a quick, accurate technique with vast potential for monolithic integration due to the absence of moving parts [27]. Nowadays, tunable frequency combs are the major limitation in terms of the resolution and sensitivity [17]. Hence, studies in the field of coherent techniques for frequency combs can improve their future performance.

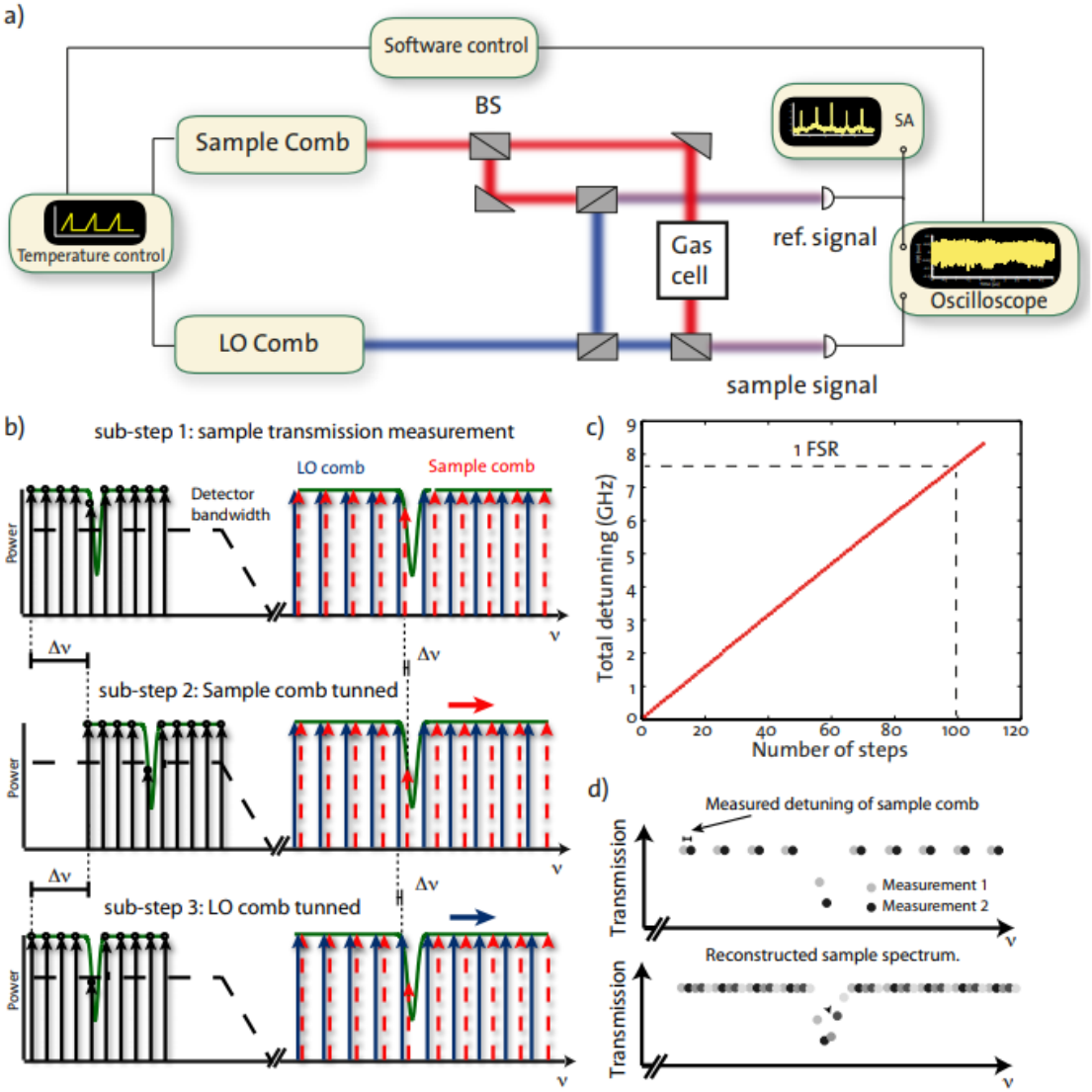

Figure 1.8: Scanning method for spectral resolution improvements. a) Schematic view of dual comb spectrometer, b) Illustration of 3 sub-steps, that form single transmission spectrum in both domains, c) Measured dependence of number of steps on total detuning, d) Reconstruction of spectrum. Figure is taken from [65].

2. Instruments

This chapter concerns with the simulation software for the QCL technology. These tools contribute significantly to the current research progress and are expected to cover even broader part of scientific work in the future. The available computational power increases each year and the technological methods evolve rapidly. Nowadays, some sort of simulation work can be found in almost every scientific paper. For this sake, it became almost indispensable.

The motivation for the development of simulation tools is the demand for information, which is difficult or too time consuming to measure experimentally. In case of the QCL technology, the most common tools are electron transport calculations and optical wave formation inside the cavity. This thesis aims on the second one in respect to the frequency comb generation and coherent control. For this purpose, TWM developed at TU Wien in 2019 has been extended by optical injection functionality. First section describes extended TWM model, giving the background for self-starting mode locking and optical injection locking simulations. Other section supplements this work with the wave-guiding model of the ridge architecture, determining the range of some important parameters used in the TWM, including GVD.

2.1 Travelling wave model

This section is divided into three parts. First describes the motivation for TWM development, presenting ideas about comb generation from early days to the present. Next part shows solutions, that lead to accurate representation of comb generation. Last part outlines the numerical implementation, that leads to the simulation software.

2.1.1 Motivation

After the first demonstration of generation of self-starting QCL frequency combs in 2012 [8], many researchers tried to determine the key factors, which lead to the comb generation. At first, the contribution of fast gain dynamics with SHB was found to be responsible for multimode behaviour [32] in Fabry-Perot cavity, leading to the comb generation with approximately constant intensity. Unfortunately, it remained unclear why some lasers generate combs, while others stay in unlocked regime regardless of the time of observation or simulation. Follow-up studies have shown that the nonlinear processes were responsible for different efficiencies of phase coupling in four-wave mixing [57]. For this sake, those nonlinearities were inspected in detail. Subsequent studies suggested, GVD values around zero are necessary for comb generation [66] and many researchers designed their devices in order to meet this condition [8, 67, 68]. Luckily, a study provided in [4] depicted comb generation as an interplay between different non-

linearities, that have to be treated simultaneously. Those contributions were included into a highly optimized TWM model. Therefore, it can be used to predict their actions on frequency combs. This has been demonstrated in the same article [4].

The described instrument has still a lot of blank space uncovered. Hence, it is particularly appealing to use it for different self-starting simulations or further developments in the field of optical injection locking.

2.1.2 Theory

This thesis presents three nonlinear processes responsible for the frequency comb generation. These processes are GVD, LEF and Kerr electro-optic effect.

The Kerr electro-optic effect (Kerr effect) stands for the change of the refractive index caused by the intensity of the slowly varying EM envelope $\Delta n \propto E^2$. In the general case of wave propagating through a bulk material of III-V semiconductors, which constitute the QCL active region, a small Kerr effect can be observed in a similar manner to the Pockels effect, that is dependent on the first power of electric field $\Delta n \propto E$ [69]. However, at transitions among the intersubband quantum wells in MIR, the Kerr effect reaches values several times larger, than in the bulk [70], so the mechanism has to be completely different to the simple bond stretching in molecules.

GVD is the characteristics of every dispersive medium. It determines the frequency dispersion of the group velocity v_g. The group velocity in a waveguiding device depends on the changes of the effective wavenumber k in frequency, therefore GVD can be determined correspondingly. It is defined as:

$$GVD(\omega_0) = \frac{\partial[v_g(\omega)^{-1}]}{\partial\omega}\Big|_{\omega_0} = \frac{\partial^2 k}{\partial\omega^2}\Big|_{\omega_0}. \tag{2.1}$$

Now we return back to the set of Maxwell-Bloch equations from 1.16. While the LEF and the Kerr contribution can be directly implemented into the wave equations, with the GVD this is not the case, because the equations are using constant ω_0 and k has been used without an exact definition. This is going to be put into order in the following lines, allowing the addition of the GVD term.

First, we define the instantaneous angular frequency ω of the electric field E. According to this, the wavevector is $k(\omega) = \omega n(\omega)/c$. Since $n(\omega)$ contains a number of nonlinear contributions, $k(\omega)$ can be written in the form of the Taylor expansion:

$$k(\omega) = k(\omega_0) + \frac{\partial k}{\partial\omega}\Big|_{\omega_0}(\omega - \omega_0) + \sum_{m=2}^{\infty}\frac{k_0^{(m)}}{m!}(\omega - \omega_0)^m. \tag{2.2}$$

According to the derivations in [19], the contribution of GVD to the wave equation can be written in the form of $-i/2k''(\partial^2 E/\partial t^2)$.

In conclusion the wave equations from 1.16 can be expanded by including the Kerr effect and GVD in form of eq. 2.3 corresponding to [19]:

$$(\frac{n}{c}\frac{\partial}{\partial t} \pm \frac{\partial}{\partial z})E_\pm - i\frac{k''}{2}\frac{\partial^2 E_\pm}{\partial t^2} = i\frac{\Gamma\mu\omega_0}{n\varepsilon_0 c L_p}\eta_\pm + i\beta(|E_+|^2 + |E_-|^2)E_\pm - \frac{\alpha_w}{2}E_\pm, \tag{2.3}$$

In these two equations, we can easily spot individual terms. On the left side there are the travelling wave term and dispersion, where GVD coefficient is represented by

k''. On the right side there are the gain contribution, Kerr effect expressed by the coefficient β and losses α_w.

Maxwell-Bloch equations expanded by nonlinearities can be directly used for study of comb generation. This robust system is unfortunately very hard to interpret. If we change some parameter, it influences other equations and the whole mechanism becomes difficult to trace. Luckily, lifetimes T_{ij} are in order of ps for QCLs. Therefore, we can consider fast gain dynamics and anticipate almost instantaneous response of variables [4]. Assuming efficient extraction from lower level, we can neglect the lower level population and change the equations correspondingly. By applying the FT following with an inverse FT to multiple variables and estimating only linear response $E_{\pm}+A\ (\partial E_{\pm}/\partial t)$ for population components and quadratic response $E_{\pm}+B\ (\partial E_{\pm}/\partial t)+B^2\ (\partial^2 E_{\pm}/\partial t^2)$ for components of normalized dipole elements, the whole system can be simplified into a master equation:

$$\begin{aligned}\left(\frac{n}{c}\frac{\partial}{\partial t} \pm \frac{\partial}{\partial z}\right)E_{\pm} = {} & \frac{g(P)}{2}\left[E_{\pm} - T_2\frac{\partial E_{\pm}}{\partial t} + T_2^2\frac{\partial^2 E_{\pm}}{\partial t^2}\right] \\ & - \frac{g(P)T_g}{2T_1P_{sat}}\left[|E_{\mp}|^2E_{\pm} - (T_2+T_g)|E_{\mp}|^2\frac{\partial E_{\pm}}{\partial t}\right. \\ & \left. - (T_2+T_g)E_{\pm}E_{\mp}\frac{\partial E^*_{\mp}}{\partial t} - T_2E_{\pm}E^*_{\mp}\frac{\partial E_{\mp}}{\partial t}\right] \\ & + i\frac{k''}{2}\frac{\partial^2 E_{\pm}}{\partial t^2} + i\beta(|E_+|^2+|E_-|^2)E_{\pm} - \frac{\alpha_\omega}{2}E_{\pm},\end{aligned} \tag{2.4}$$

where T_1 expresses $(1/T_{ul}+1/T_{ug})^{-1}$, P_{sat} is the saturation power, $P = |E_+|^2+|E_-|^2$ is the normalized power and $g(P)$ is the saturated gain defined in eq. 1.13. This representation is used for simulations in the form of optimized TWM model (further only TWM). The whole derivation is rigorously described in the supplementary information of article showing capabilities and consequences of TWM [19].

In order to justify the simplifications leading to the set of eq. 2.4, we can further represent complex electric field envelopes by the real value amplitudes and phases in the form of $E_{\pm} = A_{\pm}exp(i\phi_{\pm})$ [19]. By substituting $E_{\pm}$ into eq. 1.13, reducing several minor contributions [19] and splitting real and imaginary parts, we could obtain set a of two independent equations for the amplitude and phase. Those terms have to influence each other in an FM comb. It has been shown, that the only term providing feedback from phase to amplitude comes from the quadratic response $\propto \partial^2 E_{\pm}/\partial t^2$. Thus, it is absolutely necessary to prevent chaotic behaviour [19] and it well justifies selected complexity during derivation.

The attentive reader notices, that we have not explained and implemented the LEF yet. The LEF expresses additional broadening of spectral linewidth due to the amplitude-phase coupling mechanism, when spontaneously emitted photons couple with natural distribution inside the cavity [71]. It has been found, that the LEF can be expressed as the ratio of the carrier induced changes of the refractive index and the gain and overall gain can be modified by the factor of $1+i\alpha$ [19], where α is the LEF. This term is slightly more difficult to be manipulated, as it directly modulates gain and it would make previous equations complicated for demonstration purposes.

However, we can at least update the wave eq. 2.3:

$$(\frac{n}{c}\frac{\partial}{\partial t}\pm\frac{\partial}{\partial z})E_{\pm}-i\frac{k''}{2}\frac{\partial^2 E_{\pm}}{\partial t^2}=i(1+i\alpha)\frac{\Gamma\mu\omega_0}{n\varepsilon_0 cL_p}\eta_{\pm}+i\beta(|E_+|^2+|E_-|^2)E_{\pm}-\frac{\alpha_w}{2}E_{\pm}, \quad (2.5)$$

where α represents the LEF. Due to the fast gain dynamics in QCLs, the LEF has enormous contribution to the Kerr effect [19]. This might be also the reason for measuring a significantly higher Kerr effect in MIR subbands compared to the bulk medium [70]. Original study considered the bulk Kerr effect with the GVD, observing decreasing intensity of individual modes. This study on the other hand simulates comb generation by the LEF in combination with the GVD, while the bulk Kerr effect contribution is considered to be zero.

2.1.3 Numerical implementation

TWM model defines a system, where future time step at one place inside the cavity can be calculated from the previous spatial step. The whole cavity is divided into multiple grid points N, that directly determines the number of steps to reach a single roundtrip $2N$. The calculated vector contains multiple time-dependent variables from eq. 1.16, including the forward and backward propagating electric field envelopes E_+ and E_-. These are initially set to zero for all points inside the cavity. As we know the size of one step in space L/N and time $(n/c)(L/N)$, we can discretize the master equation and iteratively calculate the values for chosen number of points.

At the end of the cavity, the electric field abruptly attenuates because of the boundary conditions on facets, that are determined from the reflection coefficient $r=\sqrt{R}$, where R is the cavity reflectance. Usually both facets are modeled with the same reflectances, which results in spatially symmetric distribution of variables within the cavity. At this point, it is fair to mention, the model is also capable of ring cavity simulations and slow gain simulations, where whole set of Maxwell-Bloch equations is used instead of master equations. Since all simulations are going to be demonstrated on a Fabry-Perot QCL cavity, those examples are pushed to the side.

Electric injection locking is managed by modulating otherwise constant pumping current by time dependent sinusoidal signal at the selected area near one of the cavity facet. Newly developed optical injection locking functionality is managed by addition of electric field E_{DFB} to the right propagating envelope E_+ at the boundary point corresponding to the left facet.

The control interface, processing and post-processing methods are written in Python programming language. It benefits from its object-oriented nature and because of clear and intuitive construct, it is relatively easy to implement and understand the written code. Individual calculations, that are directly connected to the discretized master equation are optimized for higher performance. This is achieved by multithreading and calculations on the graphics processing unit instead of the conventionally used control processing unit. These time-demanding calculations are written in C programming language. Compared to the Python, compilation occurs only once and because of the low-level access to memory, code is run more efficiently. In the end, all functionalities are connected into a single program, supporting selection of parameters, running simulations and post-processing calculated data. In addition, all methods can be relatively quickly adapted for particular requirements.

Calculation output is usually saved in selected number of last roundtrips. The most important for post-processing are complex electric field envelopes E_+ and E_-, that will be referenced as the right and left propagating signal. Each signal can be Fourier-transformed into the frequency domain, shifted in frequency to ω_0 and normalized in a manner, where distance between the neighboring modes is exactly one in norm. frequency space. The FT signal will be referenced as the complex spectrum $s = s_1 + is_2$. Spectrum carries information about intensity and phase of electric field envelopes. Both phase φ and intensity E can be calculated from eq. 2.5:

$$\begin{aligned} E &= \sqrt{s_1^2 + s_2^2}, \\ \varphi &= tan^{-1}\left(\frac{s_1}{s_2}\right), \end{aligned} \tag{2.6}$$

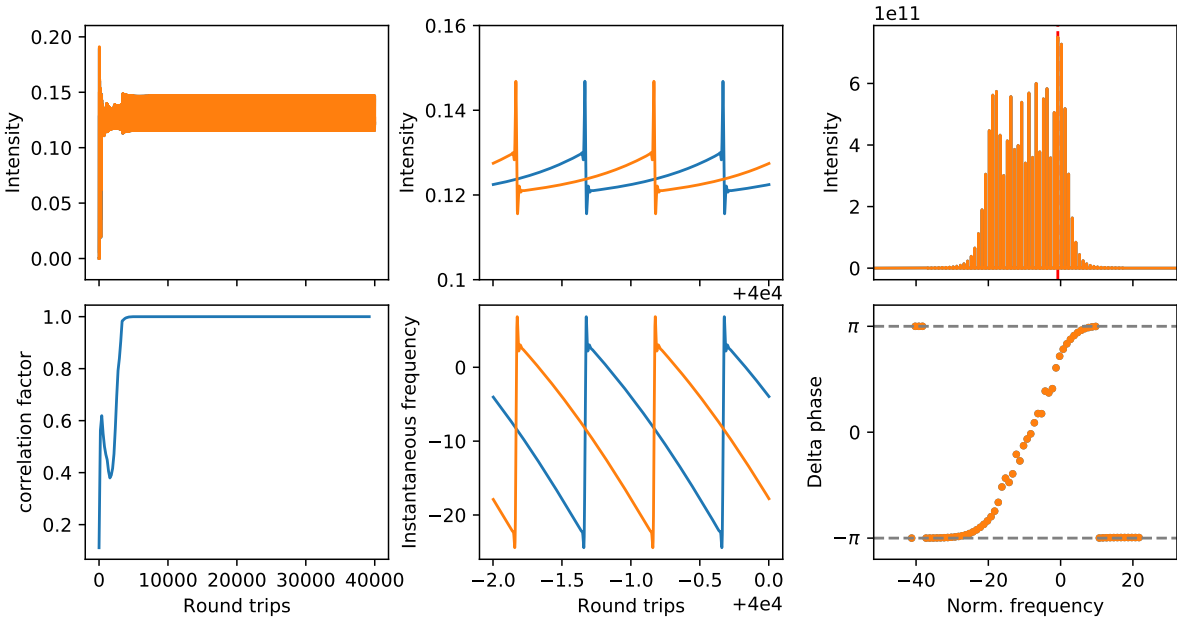

Figure 2.1: Figures of merit of generated frequency comb example for forward propagating (blue) and backward propagating (orange) electric field envelopes. Upper left figure shows the time evolution of intensity. Bottom left shows the time evolution of correlation factor. Upper middle shows the intensity during last two roundtrips. Bottom middle shows the instantaneous phase during last two roundtrips. Upper right shows the intensity spectrum and bottom right shows the delta phase distribution.

describing the modulus and phase of a complex number. Intensity and phase values are usually calculated at individual mode peaks only. Next, we define $\Delta\varphi$ (Delta phase) as the phase difference between two neighboring modes. In general, delta phases can reach any value. Because of the physical nature of phase, it can be shown in span of one period 2π, e.g. symmetric around zero, where scale is shifted to fulfil lowest frequency mode reaches $\Delta\varphi_{min} = -\pi$. Additionally, we define the correlation factor, that calculates the correlation of a selected period of signal to calculated number of periods in advance, where number of periods in advance is in range of hundreds. This value can be represented as the time evolution in respect to the roundtrips. In many cases, the whole system has to be described by single value called the locking factor.

This factor represents the average value of correlation factor in respect to the last ten roundtrips. Both correlation and locking factor show signal stability in time, which is tightly related to the phase stability and therefore, mode-locking. In our simulations, the laser is considered to be mode-locked if correlation or locking factor exceeds the value of 0.9. Operation generating lower values is considered to be in multi-mode regime, where frequency comb is not generated. Described figure of merit can be plotted in fig. 2.1.

As we can see, a frequency comb is for this case generated after approx. 5000 roundtrips, where the intensity stabilizes and correlation factor reaches value close to 1. For clear illustration purposes, a quickly locking comb has been chosen. More generally, combs can initially exhibit more chaotic behaviour, therefore, 40 000 roundtrip simulations are considered adequate. Sudden changes in intensity and instantaneous frequency are caused by reflections at the ends of cavity. Delta phases exhibit linear behaviour, which means that the modal phases follow a parabolic distribution [4]. As we can see, the information from the forward and backward propagating electric intensity envelope is equivalent and time shifted by a half of the roundtrip, therefore, it is sufficient to display only one of them. Consequently, only forward propagating components will be shown in the following pages. For the most parts of simulation study, the comb is going to be represented by the locking factor and in some cases figures of spectrum and delta phase.

2.2 Wave guiding model

TWM describes the 1D model, that traces multiple contributions of photon generation and absorption inside the AR with losses connected to mirrors. We have simplified the whole system into propagation through the gain material, where all parameters can be represented uniformly in lateral and growth direction. This assumption is absolutely necessary because of the computing requirements, which would increase significantly for the 2D and even more for the 3D. As a result, the current computing capacity is sufficient for 1D simulations only. However, there is multi-dimensional solution to this problem. If we assume all parts of the ridge laser to serve as a waveguide and we simplify AR into the state, with no emission or absorption mechanism, we can calculate the propagation constant, waveguide losses, field confinement to the AR and GVD for every existing transversal EM mode. This is called the modal analysis and it degenerates system by 1 dimension assuming geometry is uniform in wave propagation direction.

Modal analysis for 1D case in growth direction has been already developed. It is sufficient for the determination of the power confinement to the AR, but it does not have to reflect the actual waveguiding properties of the ridge laser [72], especially for structures with small ridge widths. For this case 1D mode-solving functionality has been taken over and 2D model has been implemented. This was already done as an alternative project during my Erasmus+ stay at Technical University of Vienna. However, since waveguiding properties are related to the merit of this thesis, this model was used to simulate some typical examples. In order to prevent misinterpretations, the model is going to be briefly described.

The problem solving workflow consists of the geometry creation, mesh fitting, boundaries definition and actual solving. Geometry creation is the most time consum-

ing designing step, since there are multiple atom thick layers inside AR Superlattice (SL) and even in other parts, helping to compensate stress of slightly different lattice parameters at the interface between different materials. The issue comes with the mesh creation. Neither solver can time efficiently solve the 2D problem without degeneration of thinnest layers into bigger units defined by mesh. Those units should represent the response of the system to the electromagnetic field, relative permittivity ε (from now just permittivity). Layer averaging methods are generally not trivial, but if we assume layers are sufficiently thin, we can represent each bigger unit by single anisotropic material [73]. Correct averaging method is already defined in the 1D tool. The whole 1D model is operating and calculating in Python language, hence the 2D model does the same instead of using already developed software modules, e.g. Comsol multiphysics and Lumerical Mode, where we would have to define externally calculated averaged permittivities of different layers. According to the literature [73], we can write in plane and out of plane components of averaged anisotropic permittivity in the form:

$$\begin{aligned} \varepsilon_{inPlane} &= \frac{1}{n}\sum_{i=1}^{n}\varepsilon_i, \\ \varepsilon_{outOfPlane} &= \frac{1}{\frac{1}{n}\sum_{i=1}^{n}\frac{1}{\varepsilon_i}}. \end{aligned} \tag{2.7}$$

This model uses following axis convention, where z depicts the propagation direction, y growth and x lateral direction. Since in plane and out of plane components are generally different numbers, anisotropic permittivity for single mesh point has to be defined as 3×3 matrix [74]. At first we set the non-diagonal terms to be zero. ϵ_{xx} and ϵ_{zz} diagonal terms are the in plane terms by our definition of the geometry, while ϵ_{yy} is the out of plane term. Now we can directly write the permittivity matrix:

$$\varepsilon = \begin{pmatrix} \varepsilon_{inPlane} & 0 & 0 \\ 0 & \varepsilon_{outOfPlane} & 0 \\ 0 & 0 & \varepsilon_{inPlane} \end{pmatrix}, \tag{2.8}$$

In the AR, $\mathrm{Im}(\varepsilon^2)$ is manually set to 0, since the light emission or absorption in the gain medium cannot be expressed by the imaginary part of the refractive index [40]. Thus, calculated α represents only the losses outside of the AR. In general, modal analysis is the eigenvalue problem. The eigensolver matrix is calculated inside the Vector Finite Difference Modesolver [75] from the Electromagnetic python library, that was used for exactly this purpose, since the original 'scipy' solver [76] has been replaced by the faster Krylov-Schur eigensolver [77]. The expected solution has the form:

$$\mathbf{A}(x,y,z) = \mathbf{B}(x,y)e^{-\gamma z}, \tag{2.9}$$

where $\mathbf{B}$ represents the complex amplitude of the EM field and $\gamma = \alpha + i\beta$ is the complex propagation term, β is the propagation constant and α represents the waveguide attenuation, not to be confused with the previously defined the Kerr coefficient and the LEF. β has a simple relation to the effective index $n_{eff} = \beta/k_0$ and α should be negative in the case of gain suppression. Solutions can be divided into two groups

of dominant fields, qTM (quasi-transverse magnetic), where $H_x \gg E_x \ \wedge \ E_y \gg H_y$ and qTE (quasi-transverse electric), where $E_x \gg H_x \ \wedge \ H_y \gg E_y$ [72]. Because of the parity selection rules for the intersubband transitions [78], only qTM modes are going to be concerned. In all cases, model plots $|H_x|^2$ distribution, calculated as modulus of $\mathbf{B}$ to the second power. This directly corresponds to the energy distribution inside the waveguide and it is used to calculate the energy fraction inside the AR referenced as the confinement factor Γ.

Additionally, the model received GVD functionality. GVD can be calculated from eq. 2.1, where k is represented by the propagation constant β instead. Since the calculation uses second numeric differentiation and the parameter depends on ω, the mesh has to be recreated and calculations solved for slightly lower and higher frequency too. In order to spot possible numerical instabilities, GVD is further calculated for multiple frequencies and evaluated.

3. Simulations

This is the main part of this work, where results are going to be presented. We start with the simulations of self-starting combs. This is important as we are going to see contributions of individual parameters to the frequency comb generation. The next part presents results from the waveguiding model for conventionally used Fabry-Perot ridge cavities. They point out waveguiding properties including GVD, showing some typical values of initially arbitrarily chosen parameters in the previous section. The next section is devoted to the optical injection locking, a technique that can be used to coherently manipulate the entire frequency comb, which is the current area of interest of many researchers.

3.1 Self-starting frequency combs

Many different parameters influence existence, stability, shape and other aspects of QCL frequency combs. In previous chapters we mostly discussed nonlinear terms responsible for power exchanges between different longitudinal modes, causing the self-modulation in four-wave mixing process. These nonlinearities are quite complex to start with, without knowing the behavior of the frequency comb occurrence according to other parameters. The most fundamental one is the pumping current. At first, we are going to pick some nonlinear parameters enabling comb generation. Let‘s further assume the pumping current is constant in time and space within the cavity and all carriers are used for the emission mechanism. We are going to calculate multiple states reached after 40 000 cavity roundtrips, while gradually increasing pumping current. This can be observed in fig 3.1.

The parametric sweep starts at the threshold current, as lower current generates only a weak light source dominated by spontaneous emission, that cannot produce coherent output. Just above the threshold (a), the laser supports one dominant mode at the transition frequency f_0 with 2 side modes, that are significantly lower in intensity. As a result, the generated comb is close to the single-mode regime. By increasing the applied current, the frequency comb supports more longitudinal modes, which can be seen in (b). The frequency comb then consists of multiple modes, frequency peaks have similar intensities and delta phases show linear dependence. By further increasing the pump current we observe, additional spectral broadening cannot be supported in comb regime anymore, locking factor drops and the output becomes incoherent. This is illustrated in (c). We can clearly see, that delta phases lost linear arrangement and became chaotic. In conclusion, we are going to choose broad but locked frequency combs for future simulations. The reason is, that the broad-spectrum is more beneficial for spectroscopic application. For this sake, all future simulations in this section are fixed at $J/J_{threshold} = 1.5$.

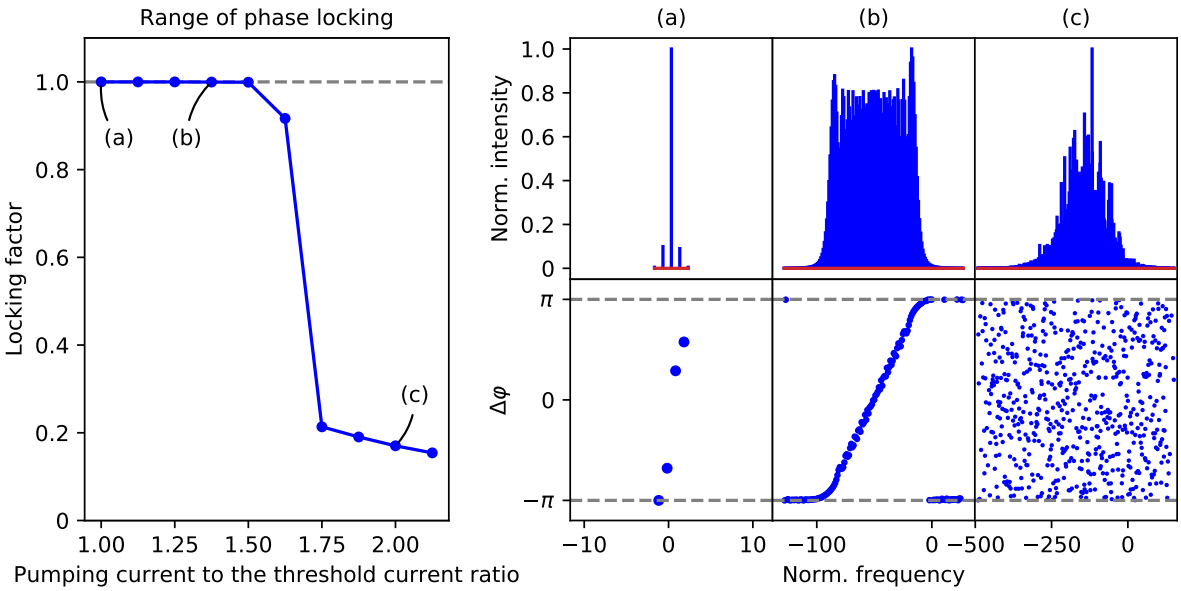

Figure 3.1: Simulation with variation in the pumping current. The left figure shows the parametric sweep of locking factor over applied current to the threshold current ratio in a range from 1 to 2.125. Different columns in the right figure show the spectral distribution of normalized intensity peaks and delta phases for selected simulations from the left figure.

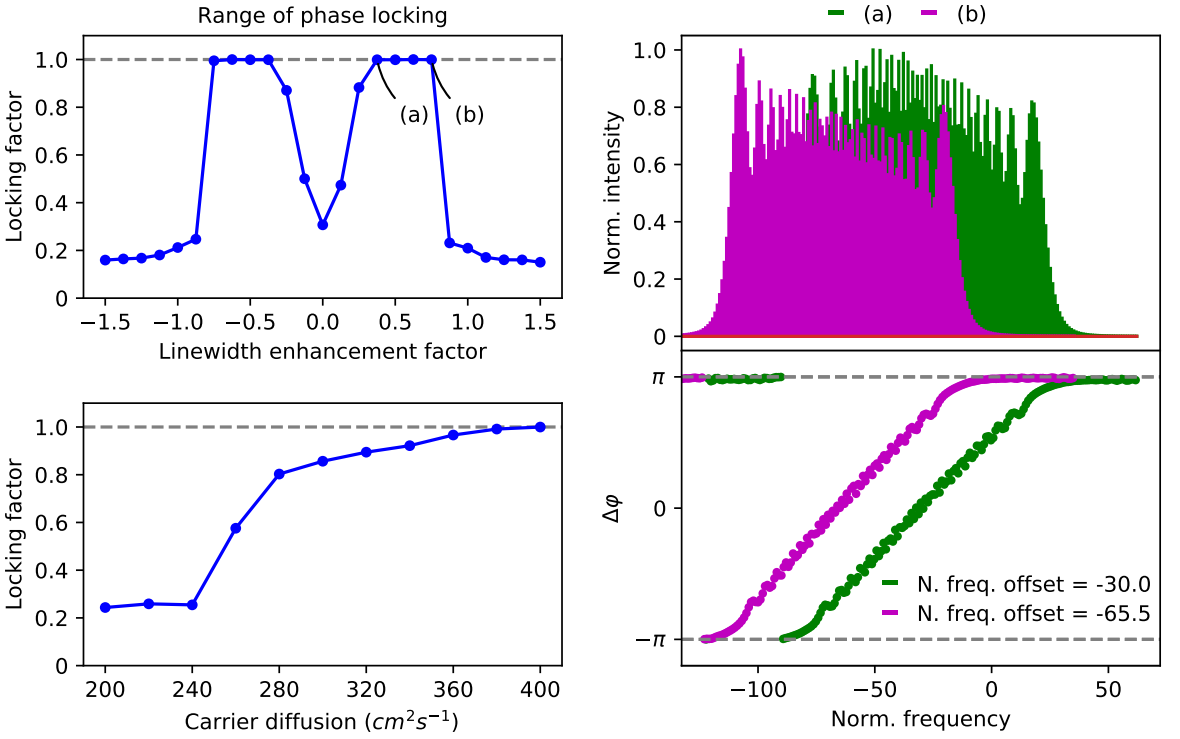

Figure 3.2: Simulation with variation in the diffusion and LEF. The upper left figure shows the parametric sweep of locking factor over LEF in a range from -1.5 to 1.5. Figures on the right show the spectral distribution of normalized intensity peaks and delta phases for LEF = 0.375 and 0.75. The lower left figure shows the parametric sweep of locking factor over diffusion in a range from 200 to 400 cm^2/s.

In the next step, we evaluate the contribution of carrier diffusion. This is simulated in fig. 3.2. The lower left plot shows, that a higher mobility results in a locked state. In the general case, the locking factor does not have to gradually grow. Yet generated output stabilizes in locked regime from certain diffusion value. The reason is, higher mobility of carriers in space reduces SHB effect [79], which is responsible for the sidemode proliferation. This means that with higher diffusion, the spectral width decreases. As a result, frequency comb with too large spectral width to be coherently supported, can be reduced and therefore, mode-locked. In this simulation, the locking factor does not change from 400 cm^2/s. In future simulations, the diffusion coefficient is set to 440 cm^2/s, although the diffusion coefficient has usually lower values in the most QCL papers [80] [79].

After the analysis of pumping current and carrier diffusion, we move towards more complex simulations. At first, we present the influence of LEF, while keeping zero GVD. The results are shown in fig. 3.2. According to the parametric sweep, there are two symmetric islands of mode-locking. Spectra for border points on the right island are shown on the left. The most evident phenomenon is, that the whole comb is negatively shifted in frequency. Frequency shift has been calculated by linear regression to the delta phases dependence, setting the central frequency to the $\Delta\varphi = 0$. It was found, that frequency comb at LEF = 0.375 is negatively shifted by 30 modes and comb at LEF = 0.75 by 65.5 modes.

In the next step, we present the influence of GVD. Fig. 3.3 shows similar results to the article [4], where locking range of GVD is studied in respect to Kerr coefficient.

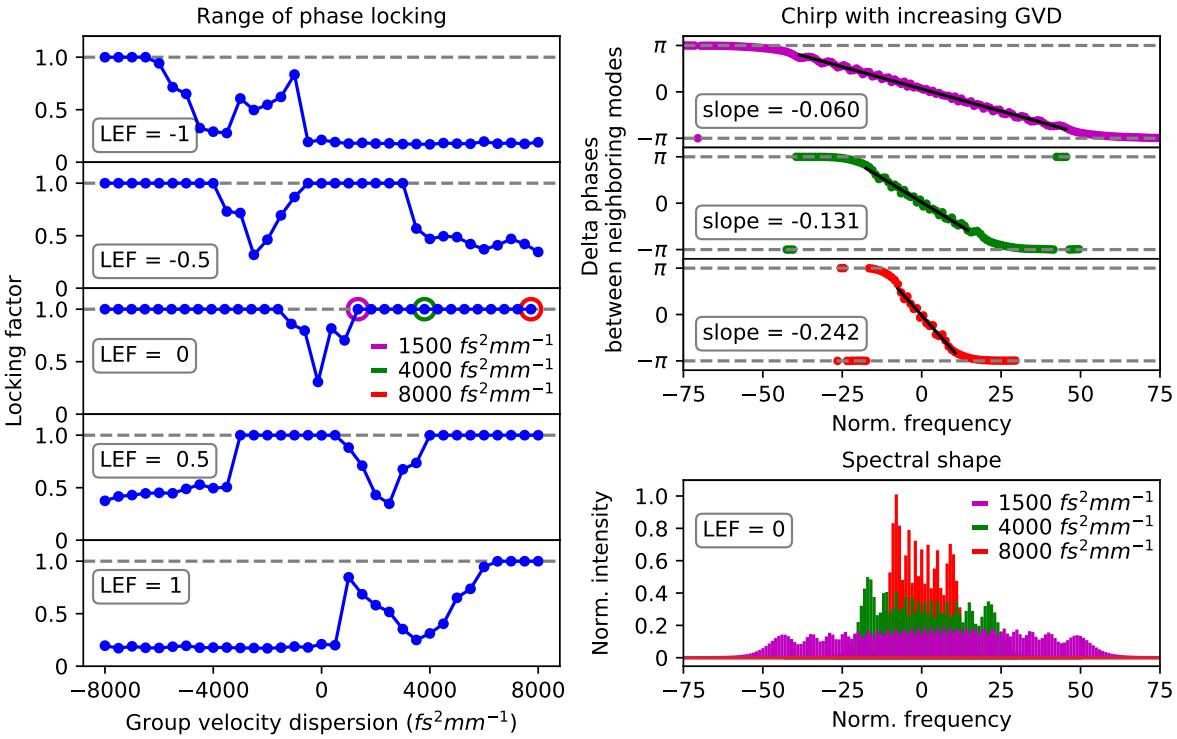

Figure 3.3: Simulation with variation in the GVD. Left figure shows the parametric sweep of locking factor over GVD in broad range from -8000 to 8000 fs^2/mm for constant LEF = -1, -0.5, 0, 0.5 and 1. Upper right figure shows delta phases for 3 different simulations at LEF = 0 and GVD = 1500, 4000 and 8000 fs^2/mm. Lower right figure shows norm. intensity spectrum for corresponding combs.

According to the figure, the locking range splits into two islands. The unlocked region between islands shifts in respect to the LEF. Those islands are expected to be infinitely long for LEF = 0. For LEF = -0.5 and 0.5, one island has finite length. For LEF = -1 and 1, same island cannot fulfil mode-locking condition anymore. In conclusion, a higher absolute value of LEF significantly limits the mode-locking range.

Restrictions in length for islands, where GVD and LEF have opposite signs has been recently observed in QCL rings [81]. The parameters of the system can be represented with contributions to the total nonlinearity and dispersion. Appropriate values of these two parameters can lead to a single-mode instability via a process called the phase turbulence, which is known across many scientific areas such as chemistry, biology and synchronization theory [82]. This process leads to multimode emission and eventually comb formation even in a ring laser cavity [81].

Similarly to another article [4], we present chirp evolution in respect to the GVD. This is shown in fig. 3.3 on the right. The chirp is represented by the slope of the regression line in delta phases on normalized frequency dependence. We can see, combs at the edge of the locking island show the most gradual chirp. As we are moving towards higher GVD, the slope gets steeper. If we examined the chirp in the left island, we would find the same dependence with positive slope values instead. Since the delta phases axis has always the same size of 2π, steeper slopes result in narrower frequency combs and vice versa. This is illustrated in the bottom right figure.

The maximum spectral width for comb operation is determined by the gain width of the laser, which is the width of the Lorentzian gain shape [83]. The slope between both islands is too small. This means that the spectral width would be too large and exceeds the available gain width of the laser. Consequently, comb operation in this region is unstable. Regardless of the spectral width, comb should be always unlocked for LEF = GVD = 0. Since this point corresponds to zero slope, hence an infinitely broad comb.

Table 3.1: Values of other parameters

Symbol	Description	Value
N_{rt}	Number of roundtrips	40 000
T_{ul}	Upper-lower level transition lifetime	0.5 ps
T_{ug}	Upper-ground level transition lifetime	3 ps
T_{lg}	Lower-ground level transition lifetime	0.08 ps
T_2	Dephasing time	0.05 ps
n	Refractive index	3.3
α_w	Waveguide power losses	2 cm^{-1}
μ	Dipole matrix element	1.7·e nm
R_l,R_r	Reflectivity of facets	0.3
Γ	Confinement factor	1
L_p	Single cascade thickness	58 nm
L	Cavity length	4 mm
λ_0	Central wavelength	8 μm

The presented results further support a hypothesis, that frequency combs can be generated in dispersion uncompensated cavities [4]. None of the conducted simulations showed a locked regime near-zero GVD exclusively. Therefore, we did not find any benefits of GVD compensation. On the other hand, prior experimental demands for

near-zero GVD values [8, 67, 68] do not have to be in contradiction. The reason is, LEF has non-zero values for laser above threshold operation [84]. This means, that the unlocked region between islands shifts according to the fig. 3.3 and zero GVD can be used to generate the frequency comb. Further, this model distinguishes between gain-induced dispersion included in gain term [85] and waveguide induced dispersion from dispersion term, while experimental works measure everything at once. Finally, the effect of higher-order terms from Taylor expansion of wavevector k, that has been neglected, might limit mode-locking for high GVDs [4].

3.2 Wave guiding simulations

In the previous section, we highlighted the interplay of LEF and GVD in self-starting frequency comb generation. Since GVD coefficient can be obtained from wave-guiding simulations, we are going to demonstratively show the influence of different ridge designs and calculate the wave-guiding parameters, including GVD for one particular device.

The device has been taken from an article [16], that uses QCLD structure for lasing and detecting functionalities, depending on the applied bias. The whole device is grown on the n-InP ($2.5 \times 10^{18} cm^{-3}$) substrate. The AR consists of InAlAs / InGaAs superlattice. Detailed information can be found directly in the article [16]. For purposes of this work, 3 different ridge designs have been tested. The mesh consists of uniformly spaced squares with a size of 100 nm. All ridges have the same height and width of 10 μm in the upper part. They are shown in fig. 3.4.

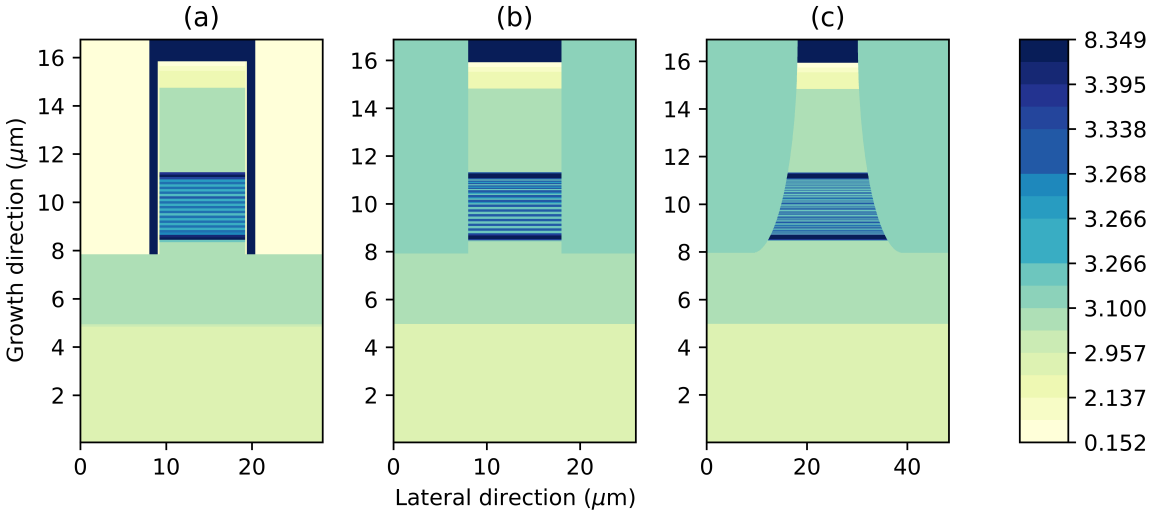

Figure 3.4: The out-of-plane component of refractive index for 3 different ridge designs. (a) represents dry-etched structure. Au at the top of the ridge provides an upper electric contact for laser biasing. As a result of fabrication, Au is also located on the ridge sides, but they are protected from a short circuit contact with a 200 nm thick SiN passivation layer. (b) shows a similar structure with compensation doped InP on the sides instead of the passivation and Au. (c) shows the previous case fabricated by wet chemical etching. Assuming perfectly isotropic etching, the profile would be circular-like.

Initially, a finite-difference modal analysis is performed for structure (a). This is

illustrated in fig. 3.5. We can clearly see, that the passivation thickness slightly influences the GVD of the fundamental qTM_{00} mode. Calculated parameters for the first 3 modes from the 2D simulation are available in table 3.3. They are further compared to the result of the 1D simulation represented in table 3.2. For visual purposes, $|H_x|^2$ components are colored alike, for both simulations. Thanks to that, it is easy to determine both qTM_{00} and qTM_{10} correspond to the TM_0 and qTM_{01} matches TM_1.

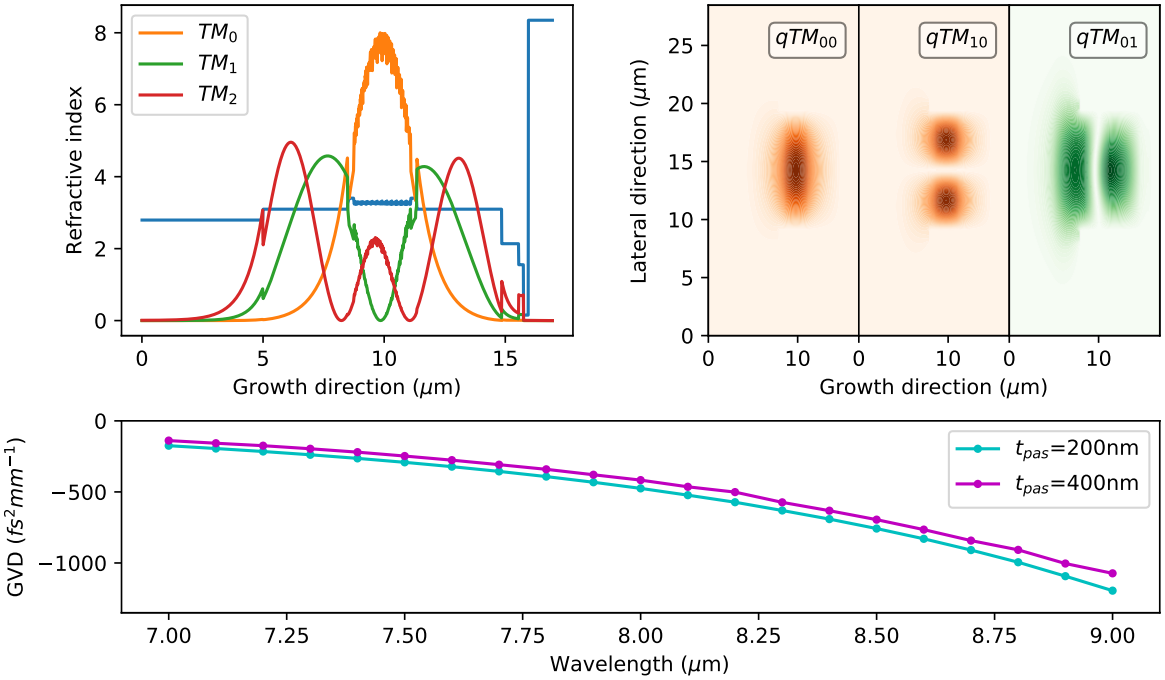

Figure 3.5: Finite-difference modal analysis of structure (a). the upper left figure shows the original 1D functionality with refractive index map in blue and the first 3 transversal modes. The upper right figure shows the 2D functionality with the first 3 modes. Both figures display $|H_x|^2$ components. Lower figure shows GVD functionality for the fundamental qTM_{00} mode demonstrated for two different passivation thicknesses of SiN.

Table 3.2: The 1D solutions of first 3 modes from modal analysis of structure (a)

mode	n_{eff}	$-\alpha$ (cm^{-1})	Γ_{AR} (%)
TM_0	3.191	1.58	63.7
TM_1	3.043	10.34	10.5
TM_2	2.944	34.16	12.2

If we first look at the table 3.2, it becomes obvious TM_0 mode is superior to the others, as energy is more tightly confined to the AR and waveguide losses are substantially lower. Corresponding modes in 2D solutions have similar values to the 1D, although AR confinement is higher and waveguide losses lower. The biggest difference between qTM_{00} and qTM_{10} mode in table 3.3 is the drop of effective index and higher waveguide losses. This effect further increases for higher-order modes. As a result, we can clearly determine the fundamental qTM_{00} transversal mode to be the most efficient. Therefore, this mode has the biggest impact on waveguiding and it can be used exclusively for the GVD calculations.

Table 3.3: The 2D solutions of first 3 modes from modal analysis of structure (a)

mode	n_{eff}	$-\alpha$ (cm^{-1})	Γ_{AR} (%)
qTM_{00}	3.172	0.97	66.8
qTM_{10}	3.103	1.62	65.8
qTM_{01}	3.024	5.96	12.5

In next step fundamental qTM_{00} mode is calculated for all 3 designs. In addition, simulation is extended by 8 μm and 12 μm wide dry-etched ridges. The GVD is further evaluated in multiple frequency calculations to account for possible numerical inaccuracy and added to the table 3.4. The most significant effect can be observed on the GVD. Initially, low negative dispersion dramatically increases for wider ridges from -799 up to -289 fs^{2}mm^{-1}. Immersed ridges on the other hand possess slightly positive GVD values. The most significant effect of wet-etching is lower confinement to AR caused by the energy shift towards lower parts, where the ridge is wider. I would like to clarify, that the GVD error has been calculated only for the immersed dry-etched ridge, where calculated GVD did not match the GVD regression in a range from 7 to 9 μm. GVD error for other cases should be one or more orders lower.

Table 3.4: The 2D solutions of qTM_{00} mode for different ridge designs. Labelling of the ridge type corresponds to the fig. 3.4

ridge type	width	n_{eff}	$-\alpha$ (cm^{-1})	Γ_{AR} (%)	GVD (fs^{2}mm^{-1})	GVD error
(a)	8 μm	3.160	1.14	66.5	-799	-
(a)	10 μm	3.172	0.97	66.8	-475	-
(a)	12 μm	3.178	0.89	66.9	-289	-
(b)	10 μm	3.180	0.80	64.9	150	$\pm$ 50
(c)	10 μm	3.189	0.77	56.0	176	-

In conclusion, we found out the waveguiding parameters of different transversal modes for ridge architecture of particular layer structure [16]. We evaluated different transversal modes and showed typical GVD values of qTM_{00} mode for different ridge designs. Those values are on the lower scale compared to the values used for the parametric sweep in fig. 3.3. No matter what, GVD could be further manipulated by dispersion tuning by the introduction of tunable optical feedback in form of an additional mirror, that is able to move outside of cavity [67]. However, we should be very careful with that, as optical feedback was found to have a negative impact on frequency comb generation [86], although a recent study in the field of electric injection locking showed, this effect can be mitigated by electric signal [61]. The effect of optical feedback on optically injection-locked signal remains unclear.

3.3 Optical injection locking

In the last part, we present simulations of optical injection locking, as has been discussed in previous chapters. A single-mode external optical signal is introduced near the frequency of selected comb mode [64]. It acts like a local oscillator, that influences the nearest mode [87]. As a result, the mode can shift in frequency. Because of the coherent nature of FM frequency combs, the whole spectrum shifts accordingly. Since we

demand coherent and easily controlled output, we should wisely choose cavity parameters for self-starting frequency combs. First, to take advantage of coherent properties, the laser cavity should be in a self-starting regime, which means the locking factor should be close to 1. Second, the laser should not have too many modes, since broad combs are more difficult to manipulate. Finally, the laser should have non-zero LEF, not only because it is more realistic but also for observation of red/blue shift difference predicted in theoretical study [88].

For a purpose of following simulations, we choose parameters from tab 3.1. Applied current to the threshold current ratio is lowered to 1.2 in order to generate a narrower comb, diffusion is set to 440 cm^2/s, LEF is set to 0.5, so the only remaining free parameter from previous sections is the GVD. In addition, there are lots of parameters of optical injection signal (referenced as DFB). First, we need to determine the injection mode. It turns out, that this numerical instability increases with the distance from the normalized frequency = 0. For this sake, all simulations are going to use the first mode to the left from the normalized frequency = 0. Bear in mind, this value slightly changes with different GVD, but in general, it is around normalized frequency = -0.77. In the next step, we accurately determine the exact peak position of the selected mode from the spectrum array of self-starting comb simulation. This is also important because the detuning frequency is in the range of MHz and an inaccurate offset could significantly shift the actual detuning.

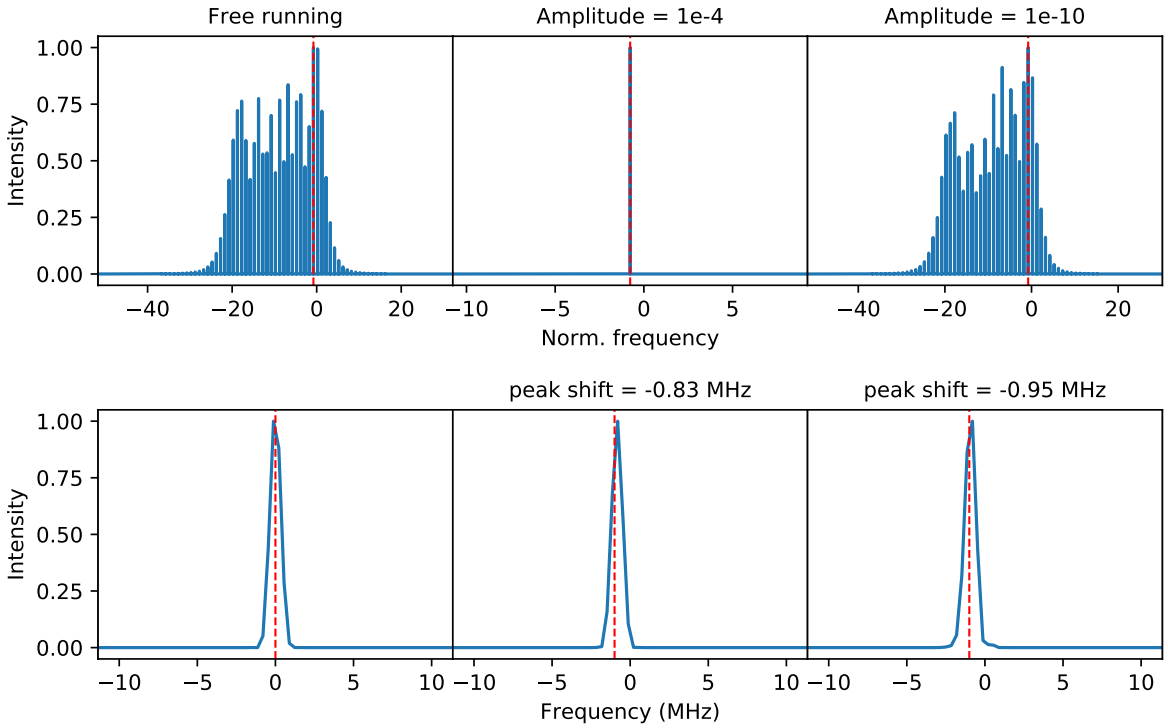

Figure 3.6: Effect of DFB amplitude upon frequency comb spectrum. The injection frequency is labeled by the red dashed line. The upper row shows an entire intensity spectrum, lower row the position of the selected mode. First column shows self-starting comb without DFB, second column the effect of E^2_{rel} = 1e-4, third column effect of E^2_{rel} = 1e-10.

From now on, we can proceed to the first simulation. We run self-starting comb simulation for 40000 roundtrips and set GVD = -2000 fs^2mm^{-1}. In the next step, we

load this simulation into the same system with an addition of DFB signal for detuning frequency ω_d = -1 MHz and two different amplitudes for another 40000 roundtrips. The results can be observed in fig. 3.6. The intensity amplitudes are presented as the relative values of DFB intensity to the saturation intensity $E^2_{rel} = E^2_0/E^2_{sat}$.

We can see, that the DFB amplitude has a huge impact on the observed intensity spectrum. Those two simulations are extreme cases, but they nicely illustrate the effect of too high or too low amplitude. A high amplitude results in other modes suppression so that the entire cavity becomes just a modulation and amplification environment for single-mode laser. A low amplitude negligibly influences the entire intensity spectrum and we can see, DFB signal is still able to capture the selected mode. However, it is beneficial to increase amplitude in future simulations to increase the locking window for higher detunings. There is also one important remark: The presented figure does not necessarily illustrate the shape of the selected intensity peak. The reason is, the recorded signal array has only a limited number of space points and they determine through FT sampling rate of spectrum in the frequency domain. In the end, low sampling frequency along with the Hann method used for signal smoothing [89] can distort the actual peak shape.

In the next step, we evaluate the action of positive and negative detuning for the constant intensity amplitude of E^2_{rel} = 1e-6. The results are shown in fig. 3.7. We can see, that the intensity spectrum gets changed significantly at this amplitude. No matter what, the generated output can be considered a frequency comb since individual modes follow the phase-locking condition.

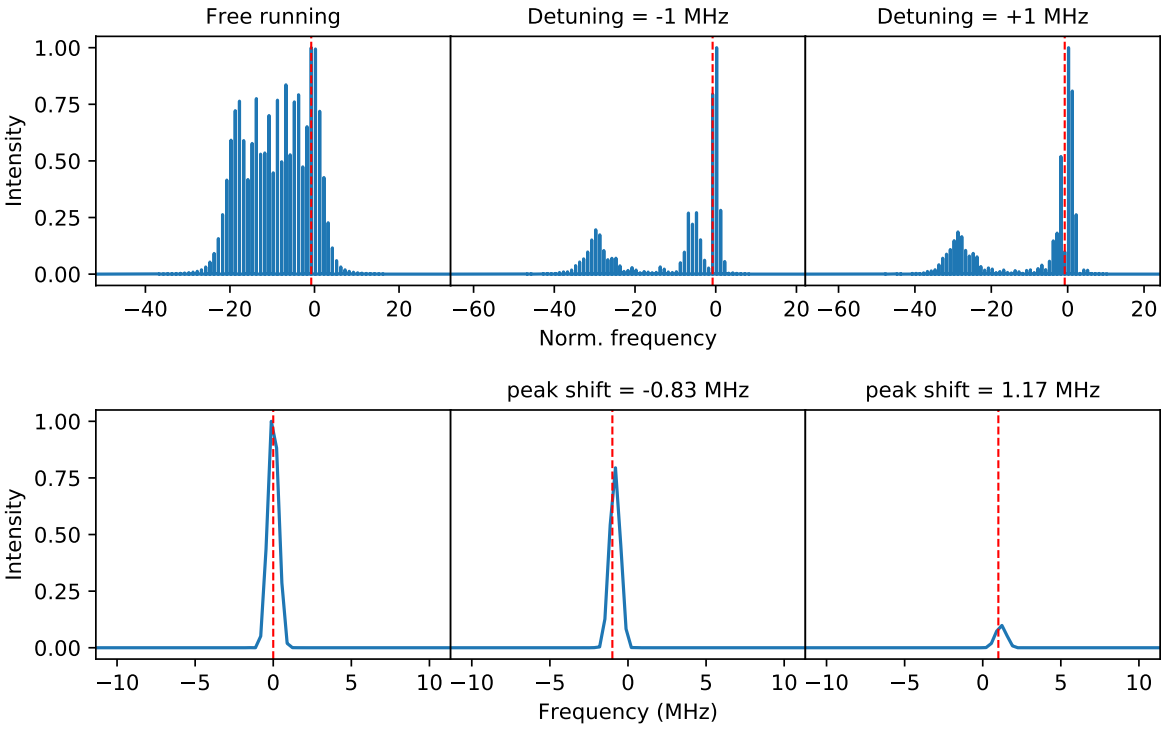

Figure 3.7: The effect of positive and negative DFB detuning upon frequency comb spectrum. The injection frequency is labeled by the red dashed line. The upper row shows an entire intensity spectrum, lower row the position of the selected mode. The first column shows self-starting comb without DFB, the second column the effect of negative detuning, the third column the effect of positive detuning.

The other important thing is, there is a major difference in spectrum intensities of individual modes (even for injected mode) for positive and negative detuning simulation. This demonstrates, that a small change in frequency with respect to the mode spacing ≈ 12 GHz, can have a major impact on the whole frequency comb.

In the last simulations, we observed the effect of a small detuning. The injected signal captured the selected mode of the frequency comb and both cavity and local oscillator coupled with each other. This does not have to be the case for larger detunings. Hence, the following simulations are going to show intensity spectra near the selected mode in respect to detuning. It requires the addition of another dimension, therefore, figures are displayed as the 2D colored array, which is shown in fig. 3.8.

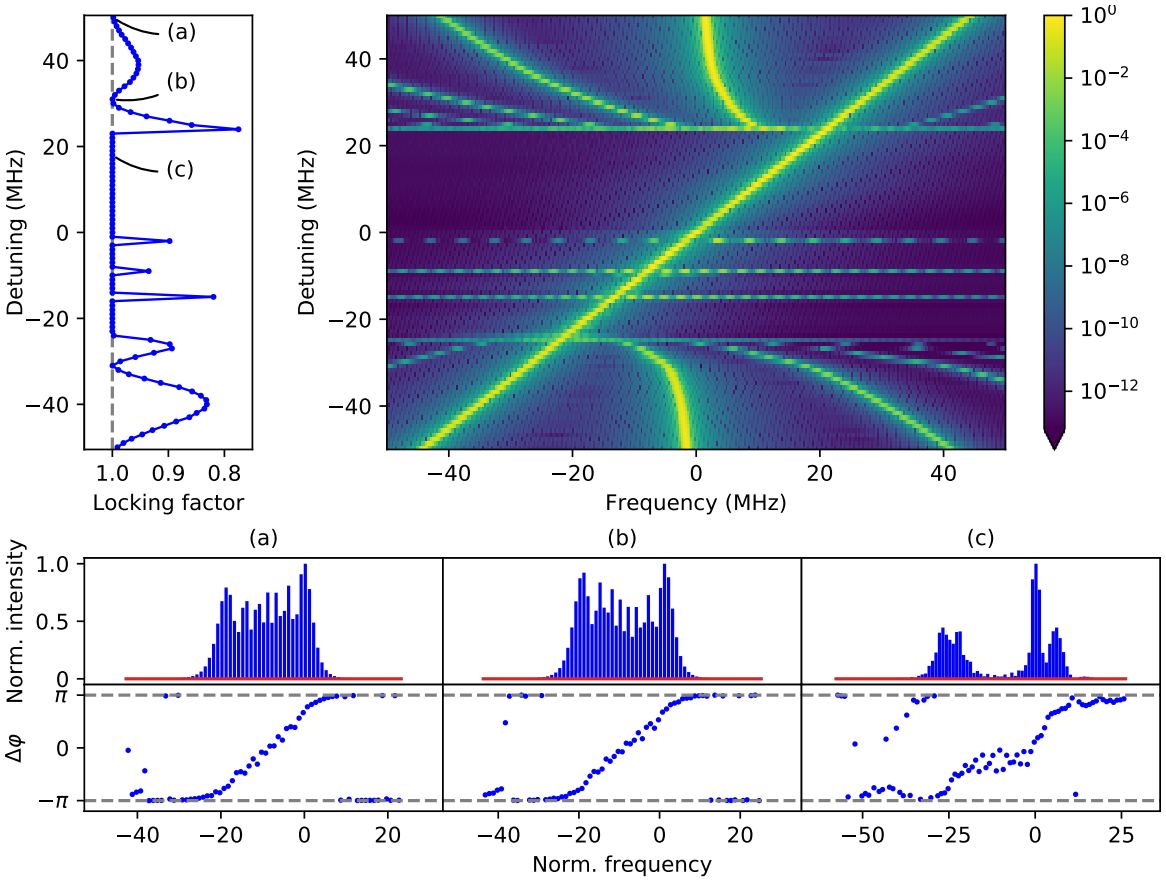

Figure 3.8: Detuning simulation for GVD = -2000 fs^{2}mm^{-1} and E^2_{rel} = 1e-6 in range from -50 MHz to 50 MHz. The upper left figure shows the parametric sweep of locking factor over detuning frequency, upper right figure the parametric sweep of spectral intensity distribution around selected mode over detuning. The bottom figures show the intensity and delta phases for selected detunings.

Each horizontal line in the colored figure represents a single simulation. The initial state for all simulations was loaded from the terminal state of 40000 roundtrips self-starting simulation without optical injection. For this sake, it represents a set of independent states pictured in (a) case of fig. 1.7. colors are in a logarithmic scale to highlight all intensity peaks. We can see, the selected mode is captured by the local oscillator in a detuning range from -24 to 23 MHz. At higher positive and lower negative detunings, oscillators suddenly separate from each other, which is accompanied by the sudden drop of the locking factor. The central peak is still strongly pulled towards the

injection signal. Further, pulling force decreases and the central peak returns back to the original position. It is really interesting, that the locking factor drops and increases again for large detunings. According to the bottom figures, comb in uncaptured regime behaves similarly to the self-starting regime without optical injection. Both (a) and (b) spectra separated by shallow unlocked island look very similar. Case (c) is on the other hand completely different. We can clearly see similarities with previous figures. After those simulations, we can generalize, injection-locked mode and neighboring peaks are overall amplified, while broader surroundings appear weaker. Interestingly, peaks located farthest away from injection frequency have a higher intensity than peaks in the middle. This is clearly caused by the choice of injection mode. Another repeating aspect relates to the delta phases. Although comb is clearly in a mode-locked regime, we cannot observe gradual chirp anymore. It rather seems like the slope of the delta phases is directly proportional to the intensity of modes. Furthermore, the delta phases between less intense modes are displaced more often.

Now, we will explain the origin of other lines in the colored figure. If we look closely at the distance between injection and central peak, we can see this distance periodically repeats in respect to other peaks. Those peaks are generated by degenerated four-wave mixing process, where one oscillator interferes twice with the second oscillator [57]. It results in the generation of frequency-shifted oscillator, where shift corresponds to the frequency difference between individual oscillators. This process is further repeated creating an evenly spaced pattern. Unlike the original longitudinal modes in frequency comb, they have higher losses. Therefore, generated peaks gradually drop in intensity. If we did not introduce a logarithmic scale, it would be even hard to spot them. A similar phenomenon can be found in few unlocked states inside the region of oscillator capturing. In conclusion, this simulation shows possibilities of coherent control, regardless of the detuning direction.

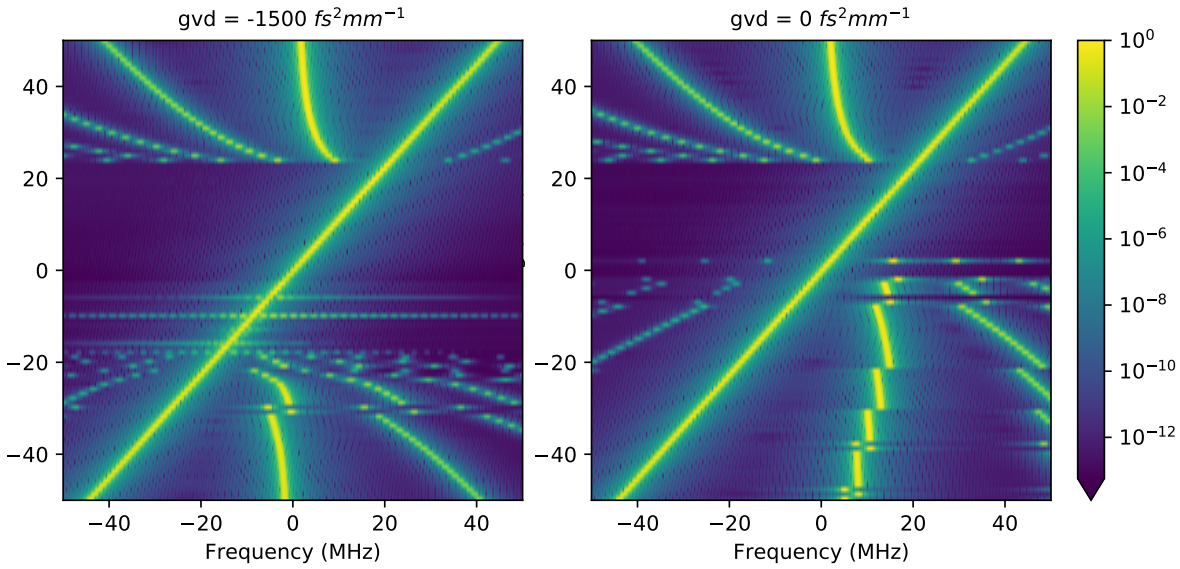

Figure 3.9: Detuning simulation for GVD = -1500 & 0 fs^2mm^{-1} and E^2_{rel} = 1e-6 in range from -50 MHz to 50 MHz. Both figures show the parametric sweep of spectral intensity distribution around selected mode over detuning.

In the following simulations in fig. 3.9 we can see, that the detuning symmetry does not apply to the GVD values closer to zero. The asymmetry is visible from GVD = -1500 fs^2mm^{-1}, where the locking window decreases for negative detuning, while in-

tensity spectra for positive detuning stay the same. In addition, at some points, we observe a sudden oscillator pushing below the locking window. The situation escalates dramatically at GVD = 0 fs^2mm^{-1}. The locking window disappears in negative detuning and pushing force prevails over pulling. For all cases, positive detuning shows the same results regardless of the GVD.

These results partially correspond to the theoretical prediction, where the intensity maximum is expected to shift towards a positive detuning value in presence of positive LEF in resonant circuit [88]. In comparison, the anti-resonant circuit should shift the intensity minimum to the negative detuning value [88]. No matter which process prevails where, it should always lead towards a shift of the locking window to the positive detuning values. The origin of sudden regular pushing in the range of uncaptured negative detuning has not been explained yet.

Finally, the progressive regime pictured in (b) case of fig. 1.7 is concerned, where the terminal state of the previous detuning simulation serves as the initial state for following detuning simulation. In order to extend the locking window as much as possible, we conduct two separate simulations for negative and positive detuning shift, while each starts at zero detuning. In the end, we combine both simulations into the colored figure. This is shown in fig. 3.10.

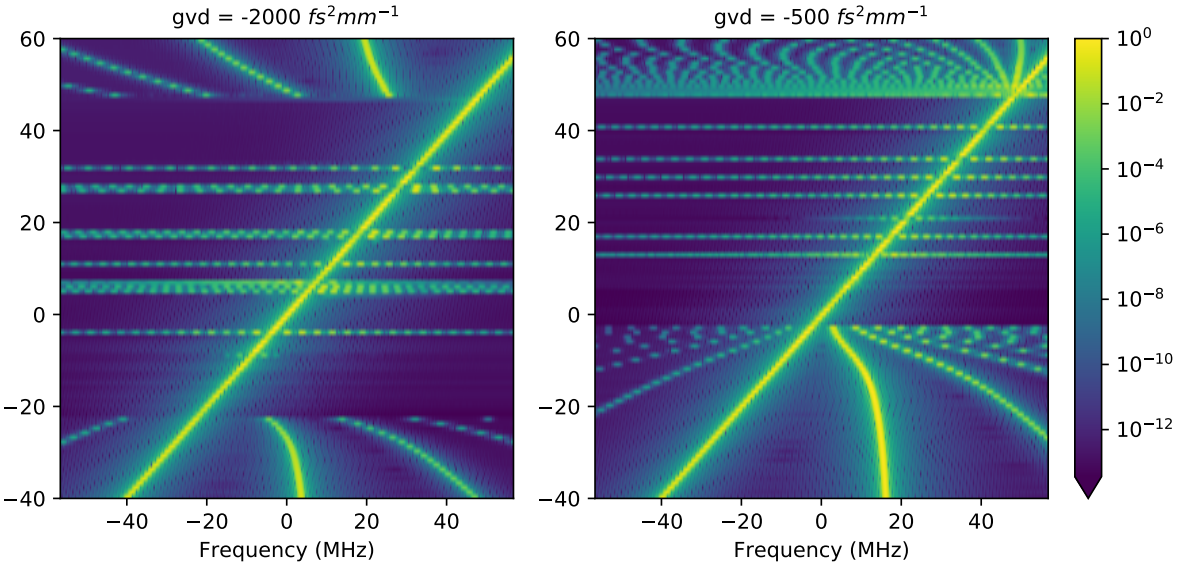

Figure 3.10: Simulation of progressive regime of detuning sweep for GVD = -2000 fs^2mm^{-1}, -500 fs^2mm^{-1} and E_{rel}^2 = 1e-6 in range from -40 MHz to 60 MHz.

In comparison to the fig. 3.9 and 3.8, we observe, that neither simulation shows sudden pushing of peaks outside the range of the locking window for negative detuning anymore. Therefore, it does not have to be considered in the actual detuning experiment, where DFB laser is sweeping through frequency. Further, there is a higher density of unlocked states inside the locking window. This can be explained by system disturbance induced by previous already disturbed detuning step. The range of the locking window is significantly extended in the range of positive detuning for both cases. At the same time, there is no apparent effect on negative detuning. For GVD = -500 fs^2mm^{-1}, that has been calculated in waveguiding simulation for 10- μm wide SiN passivated rectangular ridge architecture of QCLD design, the locking window is in range from -2 to +47 MHz. Lower GVD = -2000 fs^2mm^{-1} results into additional

capturing of negative detuning values. The locking window is in a range from -22 to +47 MHz.

This might lead to a conclusion, that the lower GVD is just better in respect to the coherent control of optical injection locking of frequency combs. However, we should not forget, that according to fig. 3.3, the lower GVD also decreases the spectral width of the frequency comb. Whereas GVD = -500 fs^2mm^{-1} creates comb with $\approx$ 60 significant modes, -2000 fs^2mm^{-1} results into the comb with $\approx$ 40 modes and -3000 fs^2mm^{-1} has just $\approx$ 25 modes, which is so few, that this detuning simulation could not be trustworthily presented, because the injected mode was often located outside the spectrum of other modes in frequency comb.

To sum it up, we successfully demonstrated the optical injection locking and discovered an enormous impact of GVD on detuning asymmetry. The detuning simulations showed, that the locking window is in the range of tens of MHz, which is in a much lower scale than the mode spacing ($f_{rep} \approx 12$ GHz). However, the possibility of coherent control of frequency combs by optical injection locking and achieved range of locking window is still considered a great success. The whole field is in the early stages of research and there are presently no scientific papers describing optical injection locking of QCL frequency combs.

Summary

This master thesis considered spatio-temporal dynamics and coherent control of QCL frequency combs. In the first part, the available highly optimized TWM tool [4] has been used for simulations of self-starting combs. The modeling approach is based on the interplay of different nonlinearities and wave dispersion in the master equation. They are responsible for coherent processes in four-wave mixing, which leads to the generation of a self-starting frequency comb. In this study, simulations were based on the interplay of GVD and LEF, while the bulk Kerr contribution was considered zero.

Initially, the effect of applied current and diffusion has been studied. Next, the GVD was considered zero and the parametric sweep of the locking factor over LEF was performed. We found out, that combs are supported in a range of two islands and LEF is responsible for the frequency shift of spectrum. Eventually, the LEF was considered constant and the parametric sweep of locking factor over GVD was performed. Results of non-zero LEF simulations shown, that combs are generally supported in a range of one infinite and one finite island, which corresponds to the article about QCL rings [81].

Moreover, the 2D finite differences EM mode solver has been used to determine waveguiding properties of different ridge architectures of particular QCLD device [16]. These properties were calculated for relevant transversal modes with the special emphasis on the GVD.

In the last part, TWM tool has been extended by optical injection locking functionality and simulations have been performed. We evaluated the effects of the amplitude of an injected signal. For high amplitudes, the cavity serves as a modulation and amplification environment for the single-mode laser. For lower values, the spectral width of the frequency comb has not been influenced and the whole comb is locked to the injected signal. In a next step, parametric sweeps over detuning have been conducted in both steady state and progressive regimes. We observed, that the range of the locking window is more limited to the positive detuning. Furthermore, this asymmetry radically increases in GVD compensated cavities. In progressive regime at LEF = 0.5 and GVD = -500, which has been calculated for 10- μm wide SiN passivated rectangular ridge laser, we simulated range of the locking window from -2 to +47 MHz.

The field of coherent control of QCL frequency combs is in the early stages of research and there are no relevant papers, that would demonstrate or describe optical injection locking of QCL combs. Hence, our pioneering simulation results can support future experimental studies, that can lead to a new class of miniaturized dual-comb spectrometers with a superior resolution and without any moving parts.

Bibliography

[1] C. Breck Hitz, J. H., James J. Ewing. *Introduction to laser technology*. Wiley-IEEE Press, 3 edn., 2004. ISBN 0471660922,9780471660927.

[2] Wolf, E. *Introduction to the Theory of Coherence and Polarization of Light*. Cambridge University Press, 2007. ISBN 978-0-521-82211-4.

[3] Burghoff, D., Yang, Y., Hayton, D. J., *et al.* Evaluating the coherence and time-domain profile of quantum cascade laser frequency combs. *Opt. Express*, 23 (2), **2015**, pp. 1190–1202. doi:10.1364/OE.23.001190.

[4] Opačak, N. and Schwarz, B. Theory of Frequency-Modulated Combs in Lasers with Spatial Hole Burning, Dispersion, and Kerr Nonlinearity. *Phys. Rev. Lett.*, 123, **2019**, p. 243902. doi:10.1103/PhysRevLett.123.243902.

[5] Jones, R. J., Moll, K. D., Thorpe, M. J., and Ye, J. Phase-Coherent Frequency Combs in the Vacuum Ultraviolet via High-Harmonic Generation inside a Femtosecond Enhancement Cavity. *Phys. Rev. Lett.*, 94, **2005**, p. 193201. doi:10.1103/PhysRevLett.94.193201.

[6] Saha, K., Okawachi, Y., Shim, B., *et al.* Modelocking and femtosecond pulse generation in chip-based frequency combs. *Opt. Express*, 21 (1), **2013**, pp. 1335–1343. doi:10.1364/OE.21.001335.

[7] Maiman, T. H. Stimulated Optical Radiation in Ruby. *Nature*, 187 (4736), **1960**, p. 493–494. doi:10.1038/187493a0.

[8] Hugi, A., Villares, G., Blaser, S., *et al.* Mid-infrared frequency comb based on a quantum cascade laser. *Nature*, 492 (7428), **2012**, pp. 229–233. doi:10.1038/nature11620.

[9] Jumpertz, L. *Nonlinear photonics in mid-infrared quantum cascade lasers*. Springer theses. Springer, 2017. ISBN 978-3-319-65879-7,3319658794,978-3-319-65878-0.

[10] Curl, R. F., Capasso, F., Gmachl, C., *et al.* Quantum cascade lasers in chemical physics. *Chemical Physics Letters*, 487 (1-3), **2010**, pp. 1–18. doi:10.1016/j.cplett.2009.12.073.

[11] Li, J., Chen, W., and Fischer, H. Quantum cascade laser spectrometry techniques: a new trend in atmospheric chemistry. *Applied Spectroscopy Reviews*, 48 (7), **2013**, pp. 523–559. doi:10.1080/05704928.2012.757232.

[12] Geiser, M., Klocke, J. L., Mangold, M., *et al.* Single-Shot Microsecond-Resolved Spectroscopy of the Bacteriorhodopsin Photocycle with Quantum Cascade Laser Frequency Combs. *Biophysical Journal*, 114 (3), **2018**, p. 173a. doi:10.1016/j.bpj.2017.11.966.

[13] Kim, S. M., Hatami, F., Harris, J. S., *et al.* Biomedical terahertz imaging with a quantum cascade laser. *Applied Physics Letters*, 88 (15), **2006**, p. 153903. doi:10.1063/1.2194229.

[14] Schwarz, B., Reininger, P., Detz, H., *et al.* A bi-functional quantum cascade device for same-frequency lasing and detection. *Applied Physics Letters*, 101 (19), **2012**, p. 191109. doi:10.1063/1.4767128.

[15] Wörle, K., Seichter, F., Wilk, A., *et al.* Breath Analysis with Broadly Tunable Quantum Cascade Lasers. *Analytical Chemistry*, 85 (5), **2013**, pp. 2697–2702. doi:10.1021/ac3030703.

[16] Schwarz, B., Wang, C. A., Missaggia, L., *et al.* Watt-Level Continuous-Wave Emission from a Bifunctional Quantum Cascade Laser/Detector. *ACS Photonics*, 4 (5), **2017**, pp. 1225–1231. doi:10.1021/acsphotonics.7b00133.

[17] Villares, G., Hugi, A., Blaser, S., and Faist, J. Dual-comb spectroscopy based on quantum-cascade-laser frequency combs. *Nature Communications*, 5 (5192), **2014**. doi:10.1038/ncomms6192.

[18] Haus, H. A theory of forced mode locking. *IEEE Journal of Quantum Electronics*, 11 (7), **1975**, pp. 323–330. doi:10.1109/JQE.1975.1068636.

[19] Opačak, N. and Schwarz, B. Theory of Frequency-Modulated Combs in Lasers with Spatial Hole Burning, Dispersion, and Kerr Nonlinearity. See Supplemental material at http://dx.doi.org/10.1103/PhysRevLett.123.243902.

[20] Sieger, M. and Mizaikoff, B. Toward On-Chip Mid-Infrared Sensors. *Analytical Chemistry*, 88 (11), **2016**, p. 5562–5573. doi:10.1021/acs.analchem.5b04143.

[21] Rothman, L., Gordon, I., Barbe, A., *et al.* The HITRAN 2008 molecular spectroscopic database. *Journal of Quantitative Spectroscopy and Radiative Transfer*, 110 (9), **2009**, pp. 533–572. doi:10.1016/j.jqsrt.2009.02.013. HITRAN.

[22] Schliesser, A., Picqué, N., and Hänsch, T. W. Mid-infrared frequency combs. *Nature Photonics*, 6 (7), **2012**, pp. 440–449. doi:10.1038/nphoton.2012.142.

[23] Yasuda, T., Yonemura, S., and Tani, A. Comparison of the Characteristics of Small Commercial NDIR CO2 Sensor Models and Development of a Portable CO2 Measurement Device. *Sensors*, 12 (3), **2012**, pp. 3641–3655. doi:10.3390/s120303641.

[24] Schwarz, B., Reininger, P., Detz, H., *et al.* Monolithically Integrated Mid-Infrared Quantum Cascade Laser and Detector. *Sensors*, 13 (2), **2013**, p. 2196–2205. doi:10.3390/s130202196.

[25] Peter Griffiths, J. A. D. H. *Fourier Transform Infrared Spectrometry*. Chemical Analysis: A Series of Monographs on Analytical Chemistry and Its Applications. Wiley-Interscience, 2nd edn., 2007. ISBN 0471194042,9780471194040.

[26] Hofstetter, D., Graf, M., Aellen, T., *et al.* 23GHz operation of a room temperature photovoltaic quantum cascade detector at 5.35 m. *Applied Physics Letters*, 89 (6), **2006**, p. 061119. doi:10.1063/1.2269408.

[27] Picqué, N. and Hänsch, T. W. Frequency comb spectroscopy. *Nature Photonics*, 13 (3), **2019**, p. 146–157. doi:10.1038/s41566-018-0347-5.

[28] Childs, D. T. D., Hogg, R. A., Revin, D. G., *et al.* Sensitivity Advantage of QCL Tunable-Laser Mid-Infrared Spectroscopy Over FTIR Spectroscopy. *Applied Spectroscopy Reviews*, 50 (10), **2015**, pp. 822–839. doi:10.1080/05704928.2015.1075208.

[29] McCreery, R. L. *Raman Spectroscopy for Chemical Analysis*. Chemical analysis 157. John Wiley 'I&' Sons, 1st edn., 2000. ISBN 9780471252870,0-471-25287-5.

[30] Schmid, T. and Dariz, P. Raman Microspectroscopic Imaging of Binder Remnants in Historical Mortars Reveals Processing Conditions. *Heritage*, 2 (2), **2019**, pp. 1662–1683. doi:10.3390/heritage2020102.

[31] Razeghi, M., Lu, Q. Y., Bandyopadhyay, N., *et al.* Quantum cascade lasers: from tool to product. *Opt. Express*, 23 (7), **2015**, pp. 8462–8475. doi:10.1364/OE.23.008462.

[32] Khurgin, J. B., Dikmelik, Y., Hugi, A., and Faist, J. Coherent frequency combs produced by self frequency modulation in quantum cascade lasers. *Applied Physics Letters*, 104 (8), **2014**, p. 081118. doi:10.1063/1.4866868.

[33] Faist, J., Capasso, F., Sivco, D. L., *et al.* Quantum Cascade Laser. *Science*, 264 (5158), **1994**, pp. 553–556. doi:10.1126/science.264.5158.553.

[34] Beck, M. Continuous Wave Operation of a Mid-Infrared Semiconductor Laser at Room Temperature. *Science*, 295 (5553), **2001**, p. 301–305. doi:10.1126/science.1066408.

[35] Gmachi, C., Capasso, F., Tredicucci, A., *et al.* Dependence of the device performance on the number of stages in quantum-cascade lasers. *IEEE Journal of Selected Topics in Quantum Electronics*, 5 (3), **1999**, pp. 808–816. doi:10.1109/2944.788454.

[36] Matsuoka, Y., Semtsiv, M. P., and Masselink, W. T. 4 - Quantum cascade lasers. IN E. Tournié and L. Cerutti (eds.), *Mid-infrared Optoelectronics*, Woodhead Publishing Series in Electronic and Optical Materials, pp. 131–179. Woodhead Publishing, 2020. ISBN 978-0-08-102709-7. doi:10.1016/B978-0-08-102709-7.00004-8.

[37] Bahaa E. A. Saleh, M. C. T. *Fundamentals of photonics*. Wiley series in pure and applied optics. Wiley, 1st edn., 1991. ISBN 0471839655,9780585321479,9780471839651.

[38] Dupont, E., Fathololoumi, S., Wasilewski, Z. R., *et al.* A phonon scattering assisted injection and extraction based terahertz quantum cascade laser. *Journal of Applied Physics*, 111 (7), **2012**, p. 073111. doi:10.1063/1.3702571.

[39] Siegman, A. E. *Lasers (Revised)*. University Science Books, hardcover edn., 1986. ISBN 0935702113,9780935702118.

[40] Wang, Y. and Belyanin, A. Active mode-locking of mid-infrared quantum cascade lasers with short gain recovery time. *Opt. Express*, 23 (4), **2015**, pp. 4173–4185. doi:10.1364/OE.23.004173.

[41] Shimoda, P. K. *Introduction to Laser Physics*. Springer Series in Optical Sciences 44. Springer-Verlag Berlin Heidelberg, 2 edn., 1986. ISBN 978-3-540-16713-6,978-3-540-38954-5.

[42] Griffiths, D. J. *Introduction to quantum mechanics*. Benjamin Cummings, 2nd edn., 2004. ISBN 9780131911758,0131911759,0131118927,9780131118928.

[43] Cui, Y. I., Harter, M. P., Dikmelik, Y., and Hoffman, A. J. Importance of coherence in models of mid-infrared quantum cascade laser gain spectra. *Journal of Optics*, 19 (9), **2017**, p. 095201. doi:10.1088/2040-8986/aa7c75.

[44] Jirauschek, C. Density matrix Monte Carlo modeling of quantum cascade lasers. *Journal of Applied Physics*, 122 (13), **2017**, p. 133105. doi:10.1063/1.5005618.

[45] Magni, V., Valentini, G., and De Silvestri, S. Recent developments in laser resonator design. *Optical and Quantum Electronics*, 23 (9), **1991**, p. 1105–1134. doi:10.1007/bf00619980.

[46] Zhigo, L., Qiao, G., and Caihua, Y. Resonator design of He-Ne laser with stabilized beam direction. *Guangxue Xuebao; (China)*, 4:8, **1984**.

[47] Yariv, A. *Quantum electronics*. Wiley, 3rd edn., 1989. ISBN 0471609978,9780471609971.

[48] Keller, U., Chiu, T., and Ferguson, J. Self-starting femtosecond mode-locked Nd: glass laser that uses intracavity saturable absorbers. *Optics letters*, 18 (13), **1993**, pp. 1077–1079. doi:10.1364/ol.18.001077.

[49] Bagheri, M., Frez, C., Sterczewski, L. A., *et al.* Passively mode-locked interband cascade optical frequency combs. *Scientific Reports*, 8 (1), **2018**. doi:10.1038/s41598-018-21504-9.

[50] Mlynczak, J. and Belghachem, N. Comparative study of the small signal gain coefficient and the dissipative losses evaluation methods of three-level microchip lasers. *Optical Materials*, 46, **2015**, pp. 93–96. doi:10.1016/j.optmat.2015.04.008.

[51] Malara, P., Blanchard, R., Mansuripur, T. S., *et al.* External ring-cavity quantum cascade lasers. *Applied Physics Letters*, 102 (14), **2013**, p. 141105. doi:10.1063/1.4800073.

[52] Meng, B., Singleton, M., Shahmohammadi, M., *et al.* Mid-infrared frequency comb from a ring quantum cascade laser. *Optica*, 7 (2), **2020**, pp. 162–167. doi:10.1364/OPTICA.377755.

[53] Schwarz, B., Ristanic, D., Reininger, P., *et al.* High performance bi-functional quantum cascade laser and detector. *Applied Physics Letters*, 107 (7), **2015**, p. 071104. doi:10.1063/1.4927851.

[54] Kosiel, K., Kubacka-Traczyk, J., Karbownik, P., *et al.* Molecular-beam epitaxy growth and characterization of mid-infrared quantum cascade laser structures. *Microelectronics Journal*, 40 (3), **2009**, pp. 565–569. doi:10.1016/j.mejo.2008.06.091. Workshop of Recent Advances on Low Dimensional Structures and Devices (WRA-LDSD).

[55] Krysa, A., Roberts, J., Green, R., *et al.* MOVPE-grown quantum cascade lasers operating at 9 m wavelength. *Journal of Crystal Growth*, 272 (1), **2004**, pp. 682–685. doi:10.1016/j.jcrysgro.2004.08.066. The Twelfth International Conference on Metalorganic Vapor Phase Epitaxy.

[56] Bai, Y., Slivken, S., Kuboya, S., *et al.* Quantum cascade lasers that emit more light than heat. *Nature Photonics*, 4 (2), **2010**, p. 99–102. doi:10.1038/nphoton.2009.263.

[57] Fok, M. and Prucnal, P. 7 - Switching based on optical nonlinear effects. IN B. Li and S. J. Chua (eds.), *Optical Switches*, Woodhead Publishing Series in Electronic and Optical Materials, pp. 181–205. Woodhead Publishing, 2010. ISBN 978-1-84569-579-8. doi:10.1533/9780857090416.181.

[58] Hillbrand, J., Auth, D., Piccardo, M., *et al.* In-Phase and Anti-Phase Synchronization in a Laser Frequency Comb. *Phys. Rev. Lett.*, 124, **2020**, p. 023901. doi:10.1103/PhysRevLett.124.023901.

[59] Razavi, B. A study of injection locking and pulling in oscillators. *IEEE Journal of Solid-State Circuits*, 39 (9), **2004**, pp. 1415–1424. doi:10.1109/JSSC.2004.831608.

[60] Piccardo, M., Kazakov, D., Rubin, N. A., *et al.* Time-dependent population inversion gratings in laser frequency combs. *Optica*, 5 (4), **2018**, pp. 475–478. doi:10.1364/OPTICA.5.000475.

[61] Hillbrand, J., Andrews, A. M., Detz, H., *et al.* Coherent injection locking of quantum cascade laser frequency combs. *Nature Photonics*, 13 (2), **2018**, pp. 101–104. doi:10.1038/s41566-018-0320-3.

[62] Kogelnik, H. and Shank, C. V. Coupled-Wave Theory of Distributed Feedback Lasers. *Journal of Applied Physics*, 43 (5), **1972**, pp. 2327–2335. doi:10.1063/1.1661499.

[63] Golka, S., Pflügl, C., Schrenk, W., and Strasser, G. Quantum cascade lasers with lateral double-sided distributed feedback grating. *Applied Physics Letters*, 86 (11), **2005**, p. 111103. doi:10.1063/1.1883332.

[64] Liu, Z. and Slavík, R. Optical Injection Locking: From Principle to Applications. *Journal of Lightwave Technology*, 38 (1), **2020**, pp. 43–59. doi:10.1109/JLT.2019.2945718.

[65] Villares, G., Hugi, A., Blaser, S., and Faist, J. Dual-comb spectroscopy based on quantum-cascade-laser frequency combs. See Supplemental material at https://www.nature.com/articles/ncomms6192.

[66] Villares, G., Riedi, S., Wolf, J., *et al.* Dispersion engineering of quantum cascade laser frequency combs. *Optica*, 3 (3), **2016**, pp. 252–258. doi:10.1364/OPTICA.3.000252.

[67] Hillbrand, J., Jouy, P., Beck, M., and Faist, J. Tunable dispersion compensation of quantum cascade laser frequency combs. *Opt. Lett.*, 43 (8), **2018**, pp. 1746–1749. doi:10.1364/OL.43.001746.

[68] Lu, Q., Razeghi, M., Slivken, S., *et al.* High power frequency comb based on mid-infrared quantum cascade laser at λ 9 μ m. *Applied Physics Letters*, 106 (5), **2015**, p. 051105. doi:10.1063/1.4907646.

[69] (Eds.), D. C. *Nonlinear Optical Properties of Organic Molecules and Crystals. Volume 1.* Quantum electronics–principles and applications. Academic Press, 1987. ISBN 978-0-12-170611-1,0121706117.

[70] Opačak, N., Cin, S. D., Hillbrand, J., and Schwarz, B. Frequency comb generation by Bloch gain induced giant Kerr nonlinearity, 2021.

[71] Henry, C. Theory of the linewidth of semiconductor lasers. *IEEE Journal of Quantum Electronics*, 18 (2), **1982**, pp. 259–264. doi:10.1109/JQE.1982.1071522.

[72] Selvaraja, S. K. and Sethi, P. *Review on Optical Waveguides.* InTech, 2018. doi:10.5772/intechopen.77150.

[73] Wood, B., Pendry, J. B., and Tsai, D. P. Directed subwavelength imaging using a layered metal-dielectric system. *Phys. Rev. B*, 74, **2006**, p. 115116. doi:10.1103/PhysRevB.74.115116.

[74] Maria L. Calvo, V. L. *Optical waveguides: from theory to applied technologies.* Optical Science and Engineering. CRC Press, 1 edn., 2007. ISBN 9781574446982,1574446983.

[75] Fallahkhair, A., Li, K. S., and Murphy, T. E. Vector Finite Difference Modesolver for Anisotropic Dielectric Waveguides. *J. Lightwave Technol.*, 26 (11), **2008**, pp. 1423–1431. doi:10.1109/jlt.2008.923643.

[76] Lehoucq, R., Sorensen, D., and Yang, C. ARPACK Users' Guide: Solution of Large Scale Eigenvalue Problems with Implicitly Restarted Arnoldi Methods. *SIAM*, , **1997**. doi:10.1137/1.9780898719628.

[77] Stewart, G. A Krylov-Schur Algorithm for Large Eigenproblems. *SIAM Journal on Matrix Analysis and Applications*, 23, **2000**. doi:10.1137/S0895479800371529.

[78] Yang, R. Q., Xu, J. M., and Sweeny, M. Selection rules of intersubband transitions in conduction-band quantum wells. *Phys. Rev. B*, 50, **1994**, pp. 7474–7482. doi:10.1103/PhysRevB.50.7474.

[79] Mansuripur, T. S., Vernet, C., Chevalier, P., *et al.* Single-mode instability in standing-wave lasers: The quantum cascade laser as a self-pumped parametric oscillator. *Physical Review A*, 94 (6), **2016**, p. 063807. doi:10.1103/physreva.94.063807.

[80] Vuković, N. N., Radovanović, J., Milanović, V., and Boiko, D. L. Low-Threshold RNGH Instabilities in Quantum Cascade Lasers. *IEEE Journal of Selected Topics in Quantum Electronics*, 23 (6), **2017**, pp. 1–16. doi:10.1109/JSTQE.2017.2699139.

[81] Piccardo, M., Schwarz, B., Kazakov, D., *et al.* Frequency combs induced by phase turbulence. *Nature*, 582, **2020**, pp. 360–364. doi:10.1038/s41586-020-2386-6.

[82] Otsuka, K. Self-induced phase turbulence and chaotic itinerancy in coupled laser systems. *Physical review letters*, 65 (3), **1990**, p. 329. doi:10.1103/physrevlett.65.329.

[83] Gallion, P. and Debarge, G. Quantum phase noise and field correlation in single frequency semiconductor laser systems. *IEEE Journal of Quantum Electronics*, 20 (4), **1984**, pp. 343–349. doi:10.1109/jqe.1984.1072399.

[84] Jumpertz, L., Michel, F., Pawlus, R., *et al.* Measurements of the linewidth enhancement factor of mid-infrared quantum cascade lasers by different optical feedback techniques. *AIP Advances*, 6 (1), **2016**, p. 015212. doi:10.1063/1.4940767.

[85] Parz, W., Müller, T., Darmo, J., *et al.* Intersubband gain-induced dispersion. *Opt. Lett.*, 34 (2), **2009**, pp. 208–210. doi:10.1364/OL.34.000208.

[86] Jouy, P., Wolf, J. M., Bidaux, Y., *et al.* Dual comb operation of λ 8.2 μ m quantum cascade laser frequency comb with 1 W optical power. *Applied Physics Letters*, 111 (14), **2017**, p. 141102. doi:10.1063/1.4985102.

[87] Bordonalli, A. C., Fice, M. J., and Seeds, A. J. Optical injection locking to optical frequency combs for superchannel coherent detection. *Optics express*, 23 (2), **2015**, pp. 1547–1557. doi:10.1364/oe.23.001547.

[88] Chattopadhyay, T. and Bhattacharyya, P. Role of linewidth enhancement factor on the frequency response of the synchronized quantum cascade laser. *Optics Communications*, 309, **2013**, pp. 349–354. doi:10.1016/j.optcom.2013.08.007.

[89] Blackman, R. B. and Tukey, J. W. The measurement of power spectra from the point of view of communications engineering — Part I. *The Bell System Technical Journal*, 37 (1), **1958**, p. 185–282. doi:10.1002/j.1538-7305.1958.tb03874.x.

List of Abbreviations

AR ..... active region

CW ..... continuous-wave

DFB ..... distributed feedback

EM ..... electromagnetic

FM ..... frequency-modulated

FT ..... Fourier transform

FTIR ..... Fourier-transform infrared

GVD ..... group velocity dispersion

ICL ..... Interband cascade laser

LEF ..... linewidth enhancement factor

MIR ..... mid-infrared

QCL ..... Quantum cascade laser

QCLD ..... Quantum cascade laser and detector

SCL ..... separate-confinement layer

SHB ..... spatial hole burning

SL ..... superlattice

TW ..... travelling wave

TWM ..... travelling wave model